Targeted energy transfer in a vibro-impact cubic NES: description of regimes and optimal design

Zhenhang Wu, Manuel Paredes, Sébastien Seguy

Targeted energy transfer in a vibro-impact cubic NES: description of regimes and optimal design

Zhenhang Wu[1,*], Manuel Paredes[1], Sébastien Seguy[1]

Institut Clément Ader (ICA), 3 rue Caroline Aigle, Toulouse, 31400, France

Abstract

In this study, we address the response regimes of a novel Nonlinear Energy Sink (NES) that couples both nonlinearities (cubic nonlinearity and impact). In a non-smooth condition, the conventional multiple scales method is considered with impact condition. By identifying the occurrence of the collision, the asymptotic analysis of the equivalent cubic NES model and Vibro-Impact (VI) NES model can illustrate the fixed point of the Vibro-Impact Cubic (VIC) NES. Three types of VIC NES are described as a function of clearance length. The role of clearance length on the response regimes is provided, offering solid criteria for optimal design. Combined with the simulation results, our experimental observations prove the restraint effect of impact on the stability of the Strongly Modulated Response (SMR).

Keywords: Strongly modulated response, Nonlinear energy sink, Optimal design, Multiple nonlinearities

1. Introduction

In a real engineering environment, vibration results in damage to system structure, reduction of manufacturing accuracy, and human discomfort. Vibration control is therefore a major challenge. The conventional Tuned Mass Damper (TMD) has been widely adopted due to its reliable configuration and

*Corresponding author

Email address: zhenhang.wu@insa-toulouse.fr (Sébastien Seguy)

[1]CNRS, INSA-ISAE-Mines Albi-UPS, Université de Toulouse

low cost. However, the TMD also brings about the disadvantages of narrow frequency absorption range and large additional mass, which can be overcome by means of a Nonlinear Energy Sink (NES), a new research hotspot developed in the last two decades [1]. The NES uses the nonlinear component to substitute the linear stiffness in the additional system. According to the source of nonlinearity, it can be classified as cubic NES [2], bistable NES [3], Vibro-Impact (VI) NES [4, 5], rotary NES [6, 7] and track NES [8]. The NES possesses a wider absorbing frequency range and a lighter attached mass for 1% of the main system [9].The self-adjustable nonlinear nature of the NES results in strong robustness against the degeneration of parameters in the system [10].

The NES can produce a one-way, irreversible energy pumping process, where the energy of the primary system is transferred into the NES system and efficiently dissipated through damping [11].The activation of the Targeted Energy Transfer (TET) is required to exceed specific energy thresholds. If harmonic force is applied to the system, the Strongly Modulated Response (SMR) appears. When the system performs a SMR, the NES and Linear Oscillator (LO) vibrate in the same frequency, which is referred to as 1:1 resonance. The stability of SMR is determined by an one map problem in phase plane [12]. The Slow Invariant Manifold (SIM) can be extracted with the introduction of the Manevitch variables and Multiple Scales Method (MSM) [13], where each point on the SIM represents a certain possible periodic solution for a certain energy level. The two fold points divide the SIM into unstable and stable regions according to the Floquet theory. And the threshold amplitude for phase trajectory to cross the fold point and activate the SMR under the harmonic force is determined [14].

In addition to cubic nonlinearity, impact is also largely relevant in the NES design. In the VI NES, the ball can move freely in the cavity and the energy can be dissipated through mutual impact interaction, which has been extensively investigated [15, 16]. The asymptotic approach originally applied in the cubic NES is also useful in the VI NES. Based on the multiple-scales method, the analytical descriptions of Vibro-impact NES are given in [17, 18] analyt-

ical descriptions. Similar to the cubic NES case, VI NES exists steady-state and SMR, the chaotic strongly modulated response is identified with randomly distributed periods of resonant and non-resonant motion [19]. The SIM of VI NES has only one stable and one unstable branch. Unlike the two fold points in the cubic NES SIM, the VI NES SIM only has one fold point [9]. The response regimes of the VI NES are labelled in accordance with the classification z = p/n, where p is the number of impacts and n is the number of excitation periods T during the considered time [20]. The variation of clearance leads to five different response regimes—categorised by the value of z—that appear alternatively under external excitation [21]. The characteristic behaviour of chaos and bifurcations of the VI NES has been extensively investigated [22, 23]. The TET phenomena based on the 1:1 resonance also occurs in the VI NES, with the efficiency of VI NES being consequently investigated for transient response and forced excitation [24]. The optimal design criteria of the VI NES, as well as multiple VI NES, has been previously proposed [25].

Most current studies primarily consider the single nonlinear component effect. In fact, due to manufacturing and assembly errors, cubic NES devices often introduce other constraints—such as displacement restrictions—which can lead to tight, rigid constraint collisions, while a couple of multiple nonlinearities remain a significant challenge. The cubic NES involved in the impact effect has been studied for transient response and is known as Vibro-Impact Cubic (VIC) NES [26]. The energy percentage ceases dramatically while energy percentage of normal optimal NES possesses a longer time for resonance capture. Even in a low energy input case, which is not intensive enough to activate the TET for normal NES, the VIC NES can still dissipate the energy with a very high efficiency. Farid [27] described the VIC NES as a Hybrid Cubic Vibro-Impact (HCVI) NES for harmonic excitation, applying a canonical transformation to the Action-Angle (AA) variables to describe the response regimes in VIC NES. Two types of bifurcations were identified, respectively describing the impact boundary and critical maximum transient energy level. The coupling effect of nonlinearity and impact in the vibro-impact dual-mass damper has also been

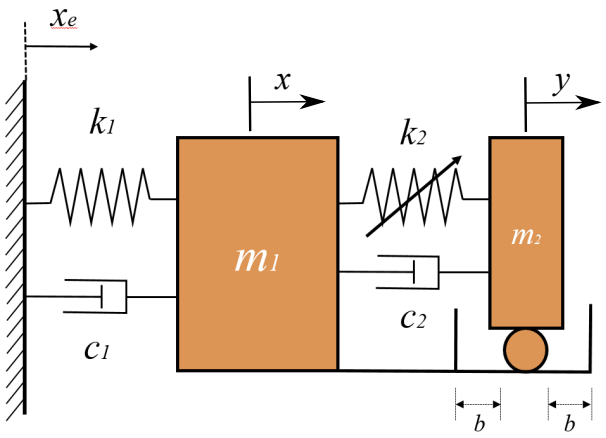

Figure 1: Diagram of Linear Oscillator (LO) the Vibro-Impact Cubic (VIC) NES system

studied [28]. The impact surfaces are added between the two auxiliary masses, one of which is supported by cubic stiffness and linear damping. The experimental result of seismic mitigation and impulsive response shows comparable control effectiveness to those of the exiting mass dampers in the optimal loading and structural situation.

Under non-smooth conditions, the conventional perturbation method is difficult to apply to those multiple nonlinearities. This study explores the potential treatments to identify the response regimes of VIC NES and provides the optimal criteria. The study is structured as follows: in Section 2, the VIC NES is modelled by multiple scales method considering impact conditions; Section 3 describes the detailed response regimes combined with the asymptotic analysis for various clearance designs; Section 4 analyses the behaviors of the VIC NES in the amplitude-frequency plan, detailing the optimal design criteria to tune the cubic NES; and Section 5 provides experimental evidence of the role of impact conditions on SMR emergence. Lastly, we highlight the most relevant conclusions.

2. Dynamic modeling

The scheme of Linear Oscillator (LO) attached with a NES is presented in Figure. 1. The NES mass m_2 is coupled with a cubic nonlinearity value k_2 and linear damping c_2. The NES mass can only move in the cavity. The clearance length on each side of the NES is bilateral and equals b. The m_1, c_1 and k_1 are the mass, viscous damping, and linear stiffness of the LO, respectively. This two-DOFs system is applied by a harmonic excitation $x_e = G\cos(wt)$. The governing equation and impact condition yield:

$$\begin{aligned} &m_1\ddot{x} + k_1 x + c_1\dot{x} + c_2(\dot{x} - \dot{y}) + k_2(x - y)^3 = k_1 x_e + c_1\dot{x}_e \\ &m_2\ddot{y} + c_2(\dot{y} - \dot{x}) + k_2(y - x)^3 = 0 \\ &\forall |x - y| < b \end{aligned} \tag{1}$$

where x and y represent the absolute displacement of the LO and NES, respectively. When the impact $|x - y| = b$ occurs, the instant displacements of the LO and NES remain constant, as does the velocity of LO. However, non-smooth dynamics bring about a sudden change in the value of the velocity of NES, as well as its direction before and after impact. This kind of non-smooth behavior entails a loss of energy. The actual velocity loss is more complex; the specific technical tool required to handle this kind of inelastic impact is developed [29] to form closed-form analytical solutions that automatically satisfy collision conditions with the energy loss. However, these simplified shock assumptions have been proven effective and useful in many VI NES problems [30, 31]. The condition of total momentum conservation gives the following equations for $|x - y| = b$:

$$\begin{aligned} &x^+ = x^-, \dot{x}^+ + \epsilon\dot{x}^+ = \dot{y}^- + \epsilon\dot{y}^- \\ &y^+ = y^-, \dot{x}^+ - \epsilon\dot{x}^+ = -r(\dot{y}^- - \epsilon\dot{y}^-) \end{aligned} \tag{2}$$

where r is the restitution coefficient (with a value between 0 and 1). The + and – superscripts represent the system parameter after and before impact. By introducing the rescaled variables Eq. (3) and substituting the new variables $v = x + \epsilon y$ and $w = x - y$, the corresponding dimensionless equations are expressed in Eq .(4).

$$\begin{aligned}
&\epsilon = \frac{m_2}{m_1}, \omega_0^2 = \frac{k_1}{m_1}, K = \frac{k_2}{m_2\omega_0^2}, \lambda_1 = \frac{c_1}{m_2\omega_0} \\
&\lambda_2 = \frac{c_2}{m_2\omega_0}, F = \frac{G}{\epsilon}, \Omega = \frac{\omega}{\omega_0}, \tau = \omega_0 t
\end{aligned} \tag{3}$$

$$\begin{aligned}
&\ddot{v} + \epsilon\lambda_1 \frac{\dot{v} + \epsilon\dot{w}}{1+\epsilon} + \frac{v + \epsilon w}{1+\epsilon} = \epsilon F \cos\Omega\tau \\
&\ddot{w} + \epsilon\lambda_1 \frac{\dot{v} + \epsilon\dot{w}}{1+\epsilon} + \frac{v + \epsilon w}{1+\epsilon} + \lambda_2(1+\epsilon)\dot{w} + K(1+\epsilon)w^3 = \epsilon F \cos\Omega t \\
&\forall |w| < b
\end{aligned} \tag{4}$$

The cavity limits the displacement of the NES with respect to the LO to no more than b. Thus, the impact condition for $|w| = b$ can be re-written as

$$\begin{aligned}
&v^+ = v^-, \dot{v}^+ = \dot{v}^- \\
&w^+ = w^-, \dot{w}^+ = -r\dot{w}^-
\end{aligned} \tag{5}$$

The Manivitch complex variables are presented to separate the fast oscillation components $\mathrm{e}^{\mathrm{i}\Omega\tau}$ and the slowly invariant amplitude components $\phi_j(\tau), j = 1, 2$ where i is the imaginary unit.

$$\begin{aligned}
&\phi_1(\tau)\mathrm{e}^{\mathrm{i}\Omega\tau} = \frac{\mathrm{d}}{\mathrm{d}\tau}v(\tau) + \mathrm{i}\Omega v(\tau) \\
&\phi_2(\tau)\mathrm{e}^{\mathrm{i}\Omega\tau} = \frac{\mathrm{d}}{\mathrm{d}\tau}w(\tau) + \mathrm{i}\Omega w(\tau)
\end{aligned} \tag{6}$$

To avoid secular terms, only terms with $\mathrm{e}^{\mathrm{i}\Omega\tau}$ are kept. The slow modulated system is obtained in Eq. (7).

$$\begin{aligned}
&\dot{\phi}_1 + \frac{\mathrm{i}\Omega}{2}\phi_1 + \frac{\epsilon\lambda_1(\phi_1 + \epsilon\phi_2)}{2(1+\epsilon)} - \frac{\mathrm{i}(\phi_1 + \epsilon\phi_2)}{2\Omega(1+\epsilon)} - \frac{\epsilon F}{2} = 0 \\
&\dot{\phi}_2 + \frac{\mathrm{i}\Omega}{2}\phi_2 + \frac{\epsilon\lambda_1(\phi_1 + \epsilon\phi_2)}{2(1+\epsilon)} - \frac{\mathrm{i}(\phi_1 + \varepsilon\phi_2)}{2\Omega(1+\epsilon)} + \frac{\lambda_2(1+\epsilon)\phi_2}{2} - \frac{3\mathrm{iK}(1+\epsilon)\phi_2^2\phi_2}{8\Omega^3} - \frac{\epsilon F}{2} = 0 \\
&\forall |\mathrm{Im}(\phi_2\mathrm{e}^{\mathrm{i}\tau})| < \Omega b
\end{aligned} \tag{7}$$

$\overline{\phi_2}$ is the conjugate value of ϕ_2, while $\mathrm{Im}(\phi_2)$ represents the imaginary part of ϕ_2 (i.e. the displacement component). The impact condition at the moment η is expressed with simple algebraic operations:

$$\begin{aligned}&\phi_1(\eta^-) = \phi_1(\eta^+)\\&\frac{\phi_2(\eta^+)\overline{\phi_2}(\eta^+) - b^2}{\phi_2(\eta^-)\overline{\phi_2}(\eta^-) - b^2} = r^2\end{aligned} \tag{8}$$

By applying the multiple scales method, the solution $\phi_j = \phi_j(\tau_0, \tau_1, \ldots)$ is expressed by the fast time scale $\tau_0 = \tau$ and the slow time scale $\tau_1 = \epsilon\tau$. The system of Eq. (7) is now examined for different orders of ϵ.

Order ϵ^0:

$$\begin{aligned}&\frac{\mathrm{d}}{\mathrm{d}\tau_0}\phi_1 = 0\\&\frac{\mathrm{d}}{\mathrm{d}\tau_0}\phi_2 + \frac{1}{2}\mathrm{i}\left(\phi_2 - \phi_1\right) + \frac{1}{2}\phi_2\lambda_2 - \frac{3}{8}\mathrm{i}K\phi_2^2\bar{\phi}_2 = 0\\&\forall|\mathrm{Im}(\phi_2\mathrm{e}^{\mathrm{i}\tau_0})| < \Omega b\end{aligned} \tag{9}$$

Order ϵ^1:

$$\begin{aligned}&\frac{\mathrm{d}}{\mathrm{d}\tau_1}\phi_1 + \frac{\mathrm{i}}{2}\left(\phi_1 - \phi_2\right) + \mathrm{i}\sigma\phi_1 + \frac{\lambda_1}{2}\phi_1 - \frac{F}{2} = 0\\&\frac{\mathrm{d}}{\mathrm{d}\tau_1}\phi_2 + \frac{\mathrm{i}}{2}\left(\phi_1 - \phi_2\right) + \frac{\mathrm{i}\sigma}{2}\left(\phi_1 + \phi_2\right) + \frac{\lambda_1}{2}\phi_1 + \frac{\lambda_2}{2}\phi_2 - \frac{3\mathrm{i}K(1-3\sigma)}{8}\phi_2^2\left|\phi_2\right| - \frac{F}{2} = 0\end{aligned} \tag{10}$$

In the order ϵ^0 equation, ϕ_1 is independent of the fast time scale τ_0 and the excitation terms disappears. The new variables $\phi_1(\tau_1) = N_1 e^{\mathrm{i}\delta_1}$ and $\phi_2(\tau_1) = N_2 e^{\mathrm{i}\delta_2}$ are introduced to extract its topological structure, known as Slow Invariant Manifold (SIM), yielding:

$$Z_1 = Z_2\lambda_2^2 + Z_2 - \frac{3K}{2}Z_2^2 + \frac{9K}{16}Z_2^3 \tag{11}$$

where $Z_1 = |\phi_1|^2, Z_2 = |\phi_2|^2$. This kind of structure implies the intrinsic property of the system. SIM consists of a set of fixed points for amplitude of NES and LO for the fast time scale, and every point means the potential periodic solution. The similar structure can be found other references [14, 32] bistable NES [33] and VI NES [19]. N_{10} and N_{20} are the periodic solution of N_1 and N_2. The two singularity points $Z_{2,j}, j = 1, 2$ divide the SIM into a left–right stable branch and a middle unstable branch in Fig. 2.

When displacement constraints are present, the periodic solutions of the system behave differently from the unconstrained case. The extra periodic solution

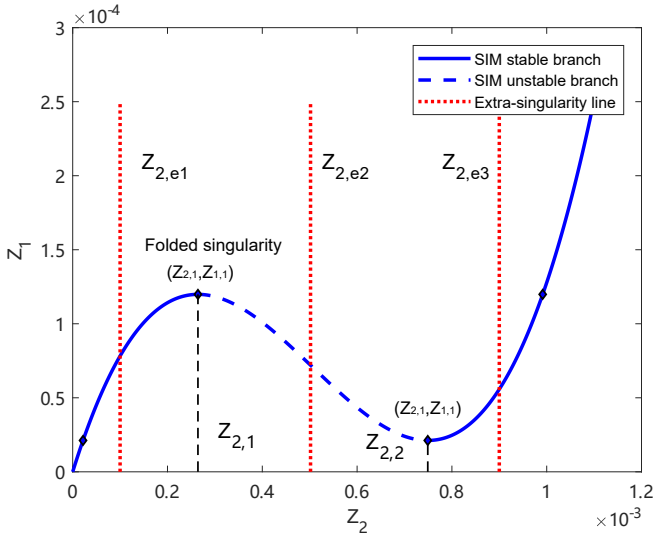

Figure 2: SIM of the VIC NES with three extra singularity lines (dotted) $Z_{2,e1}$ = 0.1e-3, $Z_{2,e2}$ = 0.5e-3, $Z_{2,e3}$ = 0.9e-3. The dashed line indicates the unstable region and the solid lines indicate the stable branches.

is considered to be introduced by an extra singularity value $Z_{2,e}$. This kind of singularity is independent of $Z_{2,j}$ and is determined by the clearance length. Consequently, it is natural to consider the different $Z_{2,e}$ locations in the SIM structure.

$$\begin{aligned} Z_{2,j} &= N_{2,j}^2 = \frac{4(2 \mp \sqrt{1-3\lambda_2^2})}{9K}, j = 1, 2 \\ Z_{2,e} &= N_{2,e}^2 = b^2 \end{aligned} \tag{12}$$

3. Response regimes

The location of the extra singularity line in the SIM structure affects the response regimes significantly. SMR as en effective vibration mitigation method, it is also determined by the various clearance lengths. SMR exists in the vicinity of the exact 1:1 resonance. The folded singularities gives necessary amplitude condition for SMR occurance [12]. The stability of one SMR cycle can be transfered into an 1-D mapping problem. Jumping phenomen, the phase trajectory

crosses folded singularities $(Z_{2,1}, Z_{1,1})$ and jumps from the left SIM branch to right SIM branch, is en essential symbol and it appears a sudden augement of NES amplitude. This process can be interrupted by the existence of clearance.

When clearance length $b<N_{2,1}(b^2<Z_{2,1})$, the extra-singularity line is located on the left stable branch. The phase trajectory can not reach folded singularity $(Z_{2,1}, Z_{1,1})$ and trigger the SMR. Therefore, this clearance design is defined as a narrow case due to that the SMR can not appear for any excitation amplitude. If the clearance length b satisfies $N_{2,1}<b<N_{2,2}(b^2<Z_{2,2})$, it means the phase trajectory has the possibility to crosse the folded singularities $(Z_{2,1}, Z_{1,1})$. However, the displacement constraint prevents phase trajectory arrives on the right stable SIM branch but extra-singularity line. When SMR disappears, the fixed point locates on the extra-singularity line instead of the right stable SIM branch. In this case, the clearance length design is considered to be modest. If $N_{2,2}<b(Z_{2,1}<b^2)$, the extra singularity line will be located on the right stable SIM branch. In this case, it is classified as a large clearance case. The clearance length does not significantly influence the critical amplitude for SMR occurrence and disappearance. The analysis of response regimes is developed according to this classification.

3.1. Narrow clearance case

If the clearance is relatively narrow (b = 10 mm), the extra singularity line crosses the left stable branch at a critical point $(Z_{2,e1}, Z_{1,e1})$; the latter $Z_{1,e1}$ is easily obtained by substituting the $Z_{2,e1}$ into Eq. (11). The simulation parameters are fixed for $\epsilon = 0.01, \lambda_1 = 1.67, \lambda_2 = 0.167$ and $K = 1742$. Those parameters are the same as reference [34]. The initial conditions for following simulations are same $v(0) = \dot{v}(0) = w(0) = \dot{w}(0) = 0$. In a low energy input case, the final stable amplitude of the NES is lower than b, which means that the NES oscillates in the cavity. In Fig. 3, the amplitude of both the NES and LO increase monotonically and ultimately reach a stable amplitude. In the subplot of Fig. 3c, the actual phase trajectory also rises along the left branch SIM monotonically without coming into contact with the extra singularity line

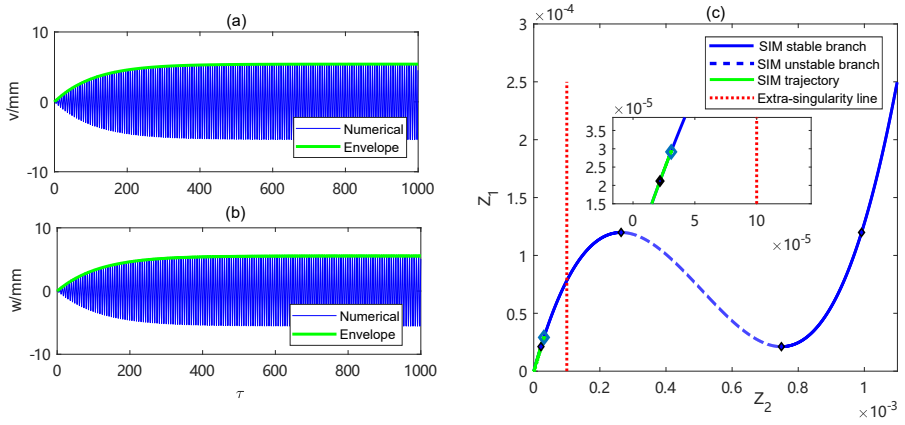

Figure 3: (a),(b) Time displacement response of v and w for narrow clearance case $G = 0.1$ mm, $\sigma = 0$. The envelopes represent the reconstructed amplitude, while the thin curves describe the time responses (c) SIM structure and phase trajectory

$Z_2 = Z_{2,e1}$.

Before the harmonic excitation amplitude causes the collision, the system behaviors can be analyzed with the framework of the cubic system. The fixed points of Eq. (7) are expressed as ϕ_{10}, ϕ_{20}. It is assumed that the imaginary part of ϕ_{20} is assumed to satisfy the displacement constraint with a low energy input. Solving the expression of ϕ_{10} in the first equation of Eq. (7) and re-substituting it into the second equation of Eq. (7) yields the expression of ϕ_{20}. Simple algebraic operations lead to the more convenient equation, with detune parameter $\Omega = 1 + \epsilon\sigma$:

$$\begin{aligned}
&\dot{\phi_1} = \dot{\phi_2} = 0, \rightarrow \phi_1(\tau) = \phi_{10}, \phi_2(\tau) = \phi_{20} \\
&\phi_{10} = \frac{\dfrac{\mathrm{i}\epsilon\phi_{20}}{\Omega(1+\epsilon)} - \dfrac{\epsilon^2\lambda_1\phi_{20}}{1+\epsilon} + \epsilon F + \mathrm{i}\epsilon^2\lambda_1 F\Omega}{\mathrm{i}\Omega + \dfrac{\epsilon\lambda_1}{1+\epsilon} - \dfrac{\mathrm{i}}{\Omega(1+\epsilon)}} \\
&\alpha_3 Z_{20}^3 + \alpha_2 Z_{20}^2 + \alpha_1 Z_{20} + \alpha_0 F^2 = 0, \quad Z_{20} = |\phi_{20}|^2
\end{aligned} \tag{13}$$

The coefficients α_1, α_2 and α_3 are determined by the system parameters. When the collision occurs, the Z_{20} reaches the extra singularity line $Z_2 = b^2$. The corresponding threshold excitation G_c can be calculated with the third

equation of Eq. (13). The excitation amplitude for impact is expressed in Eq. (14)

$$G_c = \epsilon F_c = \epsilon \sqrt{\frac{\alpha_3 K^2 b^6 + \alpha_2 K b^4 + \alpha_1 b^2}{-\alpha_0}} \tag{14}$$

Figure. 4 presents the analytical threshold excitation (surface) for various clearance designs, combined with the numerical calculations (dots). The dotted lines connect the analytical and numerical amplitude threshold and measure their differences.

When the excitation frequency equals the natural frequency of the LO ($\sigma = 0$), the required trigger excitation amplitude increases along with the clearance length design. A critical point $(Z_{2,e1}, Z_{1,e1})$ requires a more significant excitation amplitude—whose frequency is away from $\sigma = 0$—to trigger the collision conditions. When the excitation frequency is in the vicinity of its natural frequency, the resonance phenomenon will amplify the amplitude of the system, facilitating the collision condition for a low excitation amplitude. The excitation threshold G_c grows significantly when the frequency is away from the $\sigma = 0$. In the vicinity of $\sigma = 0$, the amplitude threshold values predicted by Eq. (14) are located exactly on the surface. The error increases along with the lower or higher excitation frequency. A bigger clearance design also causes a larger prediction error (indicated by the longer dotted line in Fig. 4).

It is worth mentioning that all the results resolved in this subsection are restricted to the case of narrow clearance. In this case, no SMR exists, and the impact's triggering is caused by the NES amplitude of a single fixed point exceeding b.

Once the excitation amplitude exceeds the threshold value $G_c = 0.17$ mm for case $\sigma = 0$, the impact occurs. In Fig. 5, the occurrence of impact divides the response into two parts. At the beginning, the LO and NES oscillate with a continued increasing amplitude until the NES comes into contact with the barrier. In this period, the reconstructed amplitude can accurately describe the variation of amplitude. The phase trajectory overlaps with the SIM branch

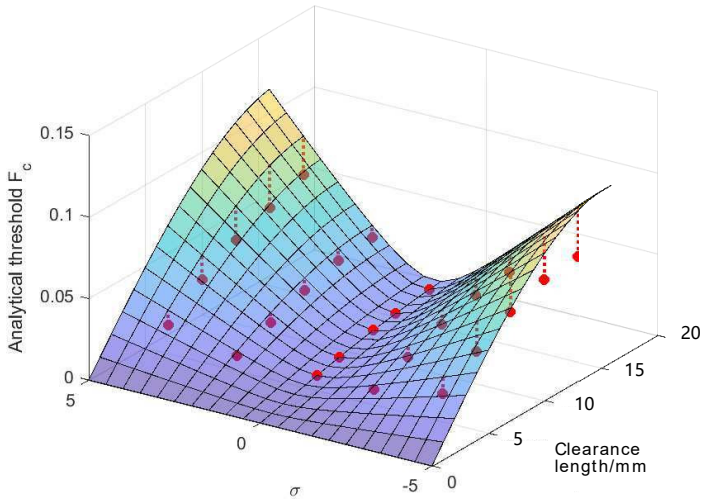

Figure 4: Analytical and numerical threshold of excitation for different clearance designs. The surface represents the analytical results. The dots are the numerical results and the dotted lines are the distance between numerical results and analytical results.

and rises in the direction of the arrow. Once the phase trajectory reaches the critical point $(Z_{2,e1}, Z_{1,e1})$, it starts oscillating and decreases along an extra singularity line. At this moment, the reconstructed amplitude cannot fit the time response of NES, for the reason that the maximal $\dot{w}$ value at the collision moment can exceed b value and is not limited by the displacement constraint. The restitution coefficient indicates the energy loss during the impact. This extra energy dissipation process leads to a decrease in the amplitude of the LO, instead of crossing the critical point $(Z_{2,e1}, Z_{1,e1})$ in a pure cubic case after the impact occurs. This discontinuity in velocity can be observed in Fig. 5c; quite similar to the pure VI NES, this discontinuity belongs to the period of two asymmetric impact per cycle.

When the NES oscillates in a small amplitude due to the displacement constraint, the local stiffness becomes extremely low near the equilibrium. The relatively low velocity of the NES also reduces the influence of the damping terms. Therefore, it is reasonable to consider the cubic nonlinearity and damping terms

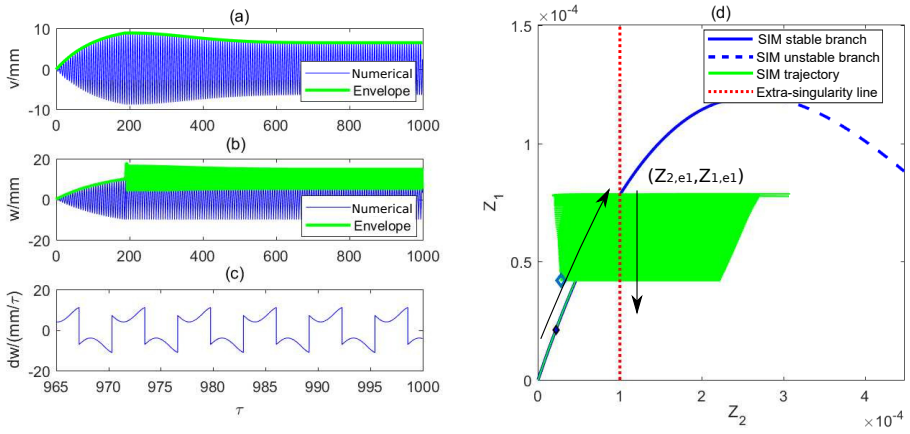

Figure 5: (a), (b) Time displacement response of v and w for narrow clearance case $G = 0.2$ mm, $\sigma = 0$. The envelopes represent the reconstructed amplitude, while the thin curves describe the time responses (c) velocity of the NES $\dot{w}$ (d) SIM structure and the phase trajectory. The solid/dashed line is a stable/unstable branch of SIM. The dotted straight line is the extra-singularity line. Arrows indicate the movement of phase trajectory before and after the impact.

$c_2(\dot{y}-\dot{x})+k_2(y-x)^3$ as a small perturbation term $O(\epsilon)$, being actually similar to a pure VI NES:

$$\begin{aligned} &m_1\ddot{x}+k_1x+c_1\dot{x}+O(\epsilon)=k_1x_e+c_1\dot{x}_e \\ &m_2\ddot{y}+O(\epsilon)=0 \\ &\forall|x-y|<b \end{aligned} \tag{15}$$

235 The following changes in variables are introduced:

$$\varepsilon=\frac{m_2}{m_1},\quad \omega_0=\frac{k_1}{m_1},\quad \tau=\omega_0 t,\quad \lambda=\frac{c_1}{m_2\omega_0},\quad \tilde{\Omega}=\frac{\Omega}{\omega_0},\quad \frac{F}{b}=\varepsilon G \tag{16}$$

After nondimensionalization, the above equation is simplified with the displacement transfer into $x = Xb, y = Yb$.

$$\begin{aligned} &\ddot{X}+\varepsilon\lambda\dot{X}+X=\varepsilon G\sin\tilde{\Omega}\tau \\ &\varepsilon\ddot{Y}=0 \\ &\forall|X-Y|<1 \end{aligned} \tag{17}$$

The impact condition gives with R represents the restitution coefficient:

$$X_+ = X_-, \quad Y_+ = Y_-, \dot{X}_+ - \dot{Y}_+ = -R\left(\dot{X}_- - \dot{Y}_-\right), \dot{X}_+ + \varepsilon\dot{Y}_+ = \dot{X}_- + \varepsilon\dot{Y}_- \tag{18}$$

In the initial time $t = 0$, the starting position is assumed to take place in the left side of the barrier. The solution for this kind of two-impacts-per-cycle regime can be expressed as follows :

$$\begin{aligned} X(t) &= \mathrm{e}^{-\frac{\varepsilon\lambda}{2}t}\left(A_1\cos\Delta t + B_1\sin\Delta t\right) + \alpha\cos(\Omega t + \eta) + \beta\sin(\Omega t + \eta) \\ Y(t) &= C_1 t + D_1, \quad 0 \le t \le t_1 \end{aligned} \tag{19}$$

t_1 represents the time of impact on the right side of the barrier, while the expressions of Δ, α, β are given in the appendix.

The analytical solution (19) of the simplified VI NES model for the various excitations case and for a frequency domain is presented in Fig. 6a,b, respectively. The parameters of the VI NES are the same as those of the VIC NES.

In Fig. 6a, the excitation amplitude starts above the impact threshold (16.7 mm) to ensure that the system has a periodic impact solution. In the narrow clearance case, the weak cubic nonlinearity and damping are neglected. The VIC NES is therefore transferred into a simpler and pure VI NES, whose analytical treatment has been well established. When the excitation grows, the analytical amplitude of the simplified model resembles the actual numerical amplitude. However, the analytical curve differs from the numerical curve once the excitation amplitude G increases to 0.3 mm. A different response regime occurs according to the classification of Peterka [35]. In this regime, there are three impacts per cycle (Fig. 7, orange curve), while the more conventional two impacts per cycle (Fig. 7, thick line) appear in the case of $G = 0.25$ mm. The reason behind a failed analytical prediction in the form of the hypothetical solution Eq. (19) can only represent the regime of two impacts per cycle.

In the frequency domain, the frequency interval σ = [-1.2 1.2] produces a discontinuous numerical curve (Fig. 6b). According to Fig. 4, when $b = 10$ mm,

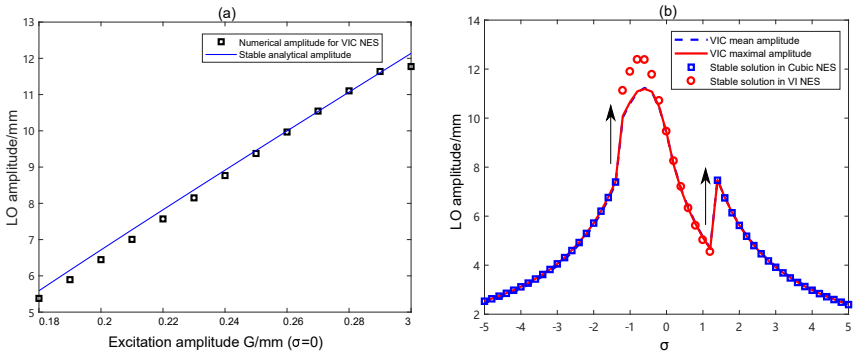

Figure 6: Comparison between the numerical response and analytical prediction (a) in growing excitation case for $\sigma = 0$ and (b) in the frequency domain for $G = 0.25$ mm

the excitation for $G = 0.25$ mm can trigger the impact motion from σ = -1 to 1.1. At this stage, the LO amplitude can be accurately predicted by the stable fixed point obtained from the VI NES model near $\sigma = 0$. The overestimations of analytical results are observed in the $\sigma <$ -0.8. The circled points in Fig. 6b are obtained through asymptotic analysis of the VI NES from Eq. (19).

When σ switches from -5 to 0, the regimes shift from the intra-cavity motion into the impact motion, causing a dramatic increase in LO amplitude. The pure cubic model dominates the stable analytical solutions that can appropriately fit the numerical results on both frequency sides of Fig. 6b. The stable solutions of the cubic NES indicated by the square are calculated through the asymptotic analysis of Eq. (13), whose stability can be determined by examining both positive and negative properties of the real part of the eigenvalue equation roots (once the perturbation is introduced).

On the basis of this discussion, it is feasible to use the VI NES model to calculate the fixed point of the VIC NES in the impact conditions near $\sigma = 0$. This alternative is possible since the VIC NES numerical solution coincides with the VI NES analytical solution. When the impact does not appear, the VIC NES performs as a cubic NES.

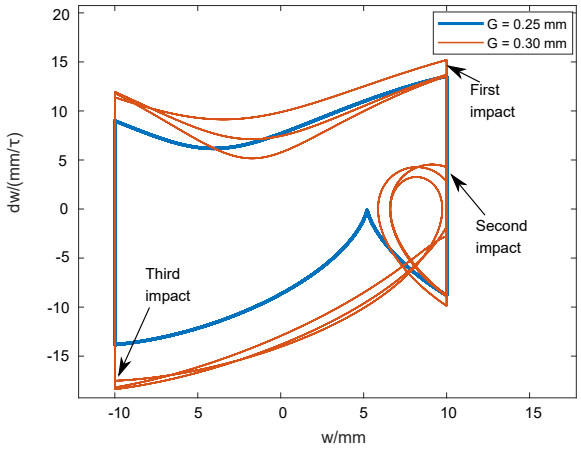

Figure 7: Phase trajectory of NES during one cycle for $G = 0.25$ mm, $\sigma = 0$ (two impacts per cycle) and $G = 0.3$ mm, $\sigma = 0$ (three impacts per cycle)

3.2. Modest clearance case

When the clearance length b is larger than the critical value $N_{2,1} = 16.3$ mm, the extra singularity line $Z_2 = Z_{2,e2}$ will be located on the unstable SIM branch. In a low energy input case (e.g. $G = 0.2$ mm in Fig. 8), the displacement has no influence on the regime of the VIC NES and no impact occurs. Therefore, the behavior of the VIC NES is the same as the pure cubic NES for the same parameters in this stage. As the amplitude of the LO and NES increase, the phase trajectory rises along the stable branch in Fig. 8c. The final state of phase trajectory (diamond in Fig. 8c) is located at a higher position before it crosses the intrinsic singularity point $(Z_{2,1}, Z_{1,1})$ due to its cubic nonlinearity.

In the pure cubic case, the relaxation-type motion occurs if the amplitude exceeds the threshold. This excitation threshold can also activate the SMR in VIC NES for the same system parameters. The typical SMR motion in a VIC NES can be classified in four stages as shown in Fig. 9d:

(1) The phase trajectory rises along with the left SIM branch. It results in both increases of LO and NES amplitudes. In this stage, the displacement constraint does not influence the oscillation in the cavity. The behaviors are the

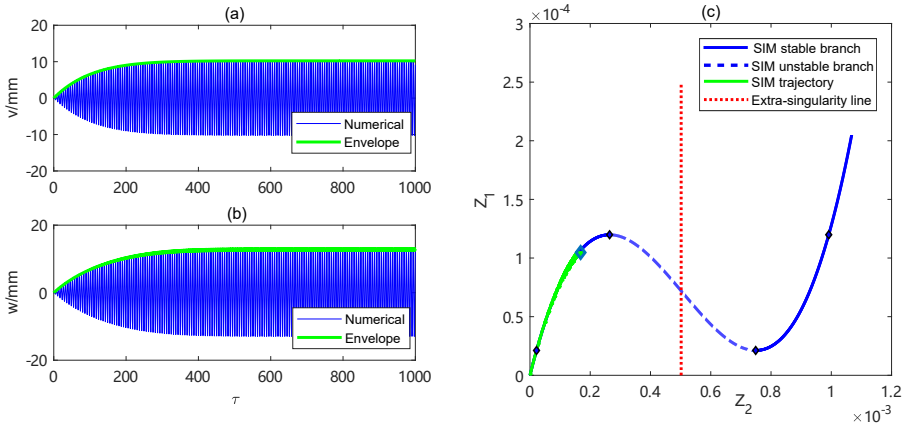

Figure 8: (a), (b) Time displacement response of v and w for modest clearance case $G = 0.2$ mm. The envelopes represent the reconstructed amplitude, while the thin curves describe the time responses (c) velocity of the NES $\dot{w}$ (d) SIM structure and the phase trajectory. The solid/dashed line is a stable/unstable branch of SIM. The dotted straight line is the extra-singularity line.

same as the cubic case.

(2) Once the phase trajectory crosses the singularity point $(Z_{2,1}, Z_{1,1})$, it triggers snap-through motion. The amplitude of NES increase dramatically; meanwhile, the LO amplitude is almost constant. The duration of this snap-through motion is short. Compared with the SMR stage of cubic NES, the phase trajectory arrives in the extra-singularity line $Z_2 = Z_{2,e2}$ instead of the right SIM branch.

(3) Due to the displacement restriction, the phase trajectory oscillates around the extra singularity line $Z_2 = Z_{2,e2}$. An efficient TET has been activated, so the LO amplitude decreases during this stage.

(4) After most energy of LO is dissipated. The LO amplitude is reduced. Another snap-through motion occurs. The phase trajectory jumps back to the left SIM branch, and it brings a reduction of NES amplitude. Then a new cycle of SMR start.

In the pure cubic case, the relaxation-type of motion occurs if the amplitude exceeds the threshold. To calculated this threshold, the second equation of order

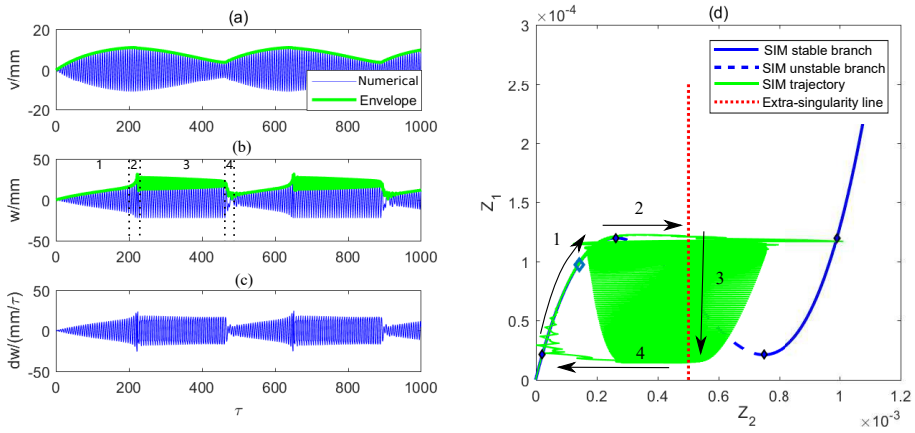

Figure 9: (a),(b) Time displacement response of v and w for modest clearance case $G = 0.25$ mm, $\sigma = 0$. The envelopes represent the reconstructed amplitude, while the thin curves describe the time responses (c) velocity of the NES $\dot{w}$ (d) SIM structure and the phase trajectory. The solid/dashed line is a stable/unstable branch of SIM. The dotted straight line is the extra-singularity line. Arrows indicate the movement of phase trajectory before and after the impact.

ϵ^0 Eq. (9) in the function of Z_2 is introduced into the first equation of order ϵ in Eq. (10). It gives Eq.(20) that contains the fixed points of the system. The Φ means the final solution of ϕ_2 when $\tau_0 \to \infty$. After substituting the variable $\phi_2(\tau_1) = N_2 e^{i\delta_2}$ into Eq.(20), the real part and imaginary part can be separated as Eq. (21).

$$\begin{aligned}&\frac{\mathrm{d}}{\mathrm{d}\tau_1}\left[2\mathrm{i}\left(-\frac{\lambda_2}{2}\Phi-\frac{\mathrm{i}}{2}\Phi+\frac{3\mathrm{i}K}{8}\Phi^2\overline{\Phi}\right)\right]\\&+2i\left(\frac{\mathrm{i}}{2}+\sigma\mathrm{i}+\frac{\lambda_1}{2}\right)\left(-\frac{\lambda_2}{2}\Phi-\frac{\mathrm{i}}{2}\Phi+\frac{3\mathrm{i}K}{8}\Phi^2\overline{\Phi}\right)-\frac{\mathrm{i}}{2}\Phi-\frac{F}{2}=0\end{aligned} \tag{20}$$

$$\frac{\mathrm{d}}{\mathrm{d}\tau_1}N_2=\frac{f_1\left(N_2,\delta_2\right)}{g\left(N_2\right)},\quad \frac{\mathrm{d}}{\mathrm{d}\tau_1}\delta_2=\frac{f_2\left(N_2,\delta_2\right)}{g\left(N_2\right)} \tag{21}$$

with

$$
\begin{aligned}
&f_1\left(N_2,\delta_2\right)=-9\lambda_1K^2N_2^5+24\lambda_1KN_2^3-12FKN_2^2\cos\delta_2\\
&-16\left(\lambda_2+\lambda_1+\lambda_2^2\lambda_1\right)+16F\cos\delta_2+16\lambda_2F\sin\delta_2\big)\\
&f_2\left(N_2,\delta_2\right)=\left(-54K^2\sigma-27K^2\right)N_2^4+\left(96K\sigma+12K-24\lambda_2\lambda_1K\right)N_2^2\\
&+36KFN_2\sin\delta_2-12\lambda_2^2-32\sigma-32\sigma\lambda_2^2+\frac{16\lambda_2F\cos\delta_2-16F\sin\delta_2}{N_2}\\
&g\left(N_2\right)=54K^2N_2^4-96KN_2^2+32+32\lambda_2^2
\end{aligned}
\tag{22}
$$

The Eq. (21) describes the slow varying amplitude part N_2 and phase part δ_2 of NES. Two types of fixed points exist: (1) ordinary fixed point for $f_1=f_2=0, g\neq 0$, (2) folds singularities for $f_1=f_2=g=0$. The second type of singularity corresponds the threshold of SMR occurs and disappears. The condition $f_1=g=0$ will cause the $f_2=0$ to be satisfied. So the expression of folds singularity is obtained as:

$$
\begin{aligned}
&\Delta_{2,j}=\arcsin\left(\frac{4\lambda_2}{\sqrt{9K^2N_{2,j}^4-24KN_{2,j}^2+16+16\lambda_2^2}}\right)\\
&\pm\arccos\left(N_{2,j}\frac{16\lambda_1-24\lambda_1KN_{2,j}^2+9\lambda_1K^2N_{2,j}^4+16\lambda_2+16\lambda_1\lambda_2^2}{4F\sqrt{9K^2N_{2,j}^4-24KN_{2,j}^2+16+16\lambda_2^2}}\right)
\end{aligned}
\tag{23}
$$

It's easy to solve the condition for latter terms in Eq. (23) and obtain the expression of force amplitude $G_{j,c}$. The threshold of SMR occurrence $G_{1,c}$ has been deduced and given by Eq. (24). From this equation, we can conclude that the SMR trigger conditions are the same for the VIC NES and the cubic NES. Because both cases share the same fold line $N_{2,1}$. However, since the other fold line $N_{2,2}$ is inaccessible in the modest clearance case, which leads to the calculation of G_2c threshold for SMR disappearance can not fit the VIC NES. And the extra singularity value $N_{2,2}=N_{2,e}=b$ is applied in Eq. (24) to obatin the threshold.

$$G_1 c = \epsilon F_{1,c} = \frac{\epsilon N_{2,1}\left(16\lambda_1 - 24\lambda_1 K N_{2,1}^2 + 9\lambda_1 K^2 N_{2,1}^4 + 16\lambda_2 + 16\lambda_1\lambda_2^2\right)}{(4\sqrt{9K^2N_{2,1}^4 - 24KN_{2,1}^2 + 16 + 16\lambda_2^2})}$$
$$G_e = \epsilon F_e = \frac{\epsilon b\left(16\lambda_1 - 24\lambda_1 K b^2 + 9\lambda_1 K^2 b^4 + 16\lambda_2 + 16\lambda_1\lambda_2^2\right)}{(4\sqrt{9K^2b^4 - 24Kb^2 + 16 + 16\lambda_2^2})} \tag{24}$$

In the cubic NES case, the analytical amplitude threshold calculated in Eq. (24) for the SMR occurs between [0.22 mm, 0.35 mm]. The numerical thresholds are [0.24 mm, 0.41 mm]. In the VIC NES, the analytical result indicates that the SMR starts and ends at [0.22 mm, 0.24 mm] by Eq. (24), while the numerical simulation found that the SMR appears between [0.24 mm, 0.28 mm]. Numerical and analytical results both confirm that the SMR starts in the same amplitude excitation cases for the VIC NES and cubic NES. The analytical predictions for SMR extinction show some differences with numerical simulation. The displacement constraint results in the SMR of the VIC NES ending at a much lower excitation amplitude case.

Figure. 10 shows the stable periodic response of the system when the excitation exceeds the force threshold. The critical force prevents the phase trajectory from jumping back to the left stable branch and being located at a similar height of singularity point $(Z_{2,2}, Z_{1,2})$, having slowly decreased along the extra singularity line $Z_2 = Z_{2,e2}$. In this critical situation, the LO amplitude possesses the minimal stable amplitude, which can only be realized in an optimal cubic NES in the larger energy input case. Thus, the displacement constraint enables the system to enter the optimization state in a lower excitation amplitude case.

As in the previous narrow clearance case, the VI model can accurately predict the fixed point of the VIC NES under impact conditions. In Fig. 11a, the system shows a stable response to impact when the excitation amplitude increases beyond 0.28 mm. In the relatively low energy case, the analytical prediction has a more significant value than the simulated one. As excitation increases, both results almost overlap.

In the frequency domain (Fig. 11b), impact appearance separates the nu-

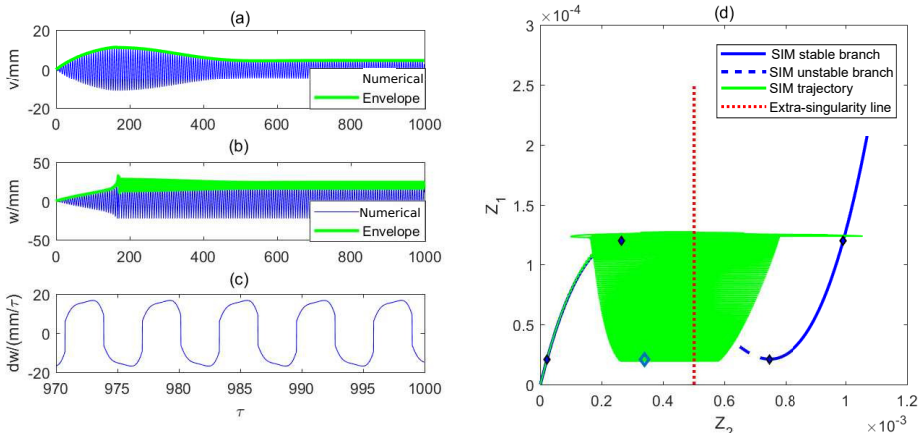

Figure 10: (a),(b) Time displacement response of v and w for modest clearance case G = 0.28 mm, $\sigma = 0$. The envelopes represent the reconstructed amplitude, while the thin curves describe the time response (c) velocity of the NES $\dot{w}$ (d) SIM structure and the phase trajectory. The solid/dashed line is a stable/unstable branch of SIM. The dotted straight line is the extra-singularity line. Arrows indicate the movement of phase trajectory before and after the impact.

merical frequency response into two parts. When the VIC NES performs as a cubic NES, the numerical amplitude of the VIC NES coincides with the square point on both [-5, -3.2] and [2.8, 5] σ intervals.

Unlike the narrow clearance case, the analytical predictions of pure cubic NES possess two stable fixed points and one unstable fixed point between the σ = [-3, -1.6] and [1.2, 2.6]. The lower stable LO amplitude branch better describes the numerical simulation (squares in Fig. 11b). In this stage, the NES amplitude tends to have a higher value, which means that more energy of the LO will be transferred into the NES, leading to a lower LO amplitude. Therefore, the numerical results of the LO amplitude are located on the lower stable solution branch. The intervals [-3, -1.6] with three fixed points mean that the NES possesses three potential amplitude cases. The impact is triggered due to the resonance peak, whose appearance does not strictly follow the criteria for the appearance of the three fixed points at σ = -1.6. On the other side, that of interval [1.2, 1.6], the impact is accompanied by a SMR. When the

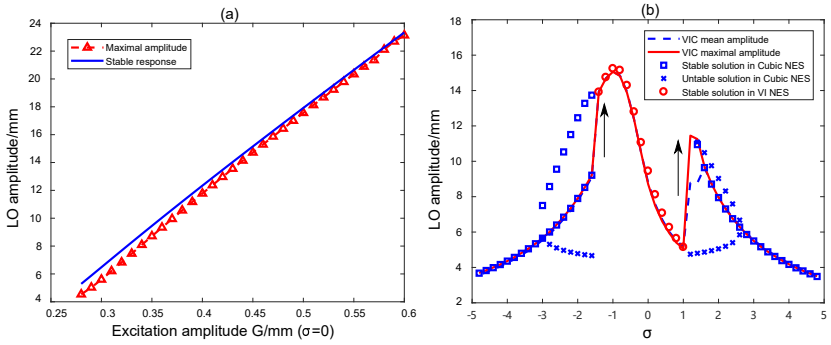

Figure 11: Comparison between the numerical response and analytical prediction (a) in the growing excitation case for $\sigma = 0$ and (b) in the frequency domain for $G = 0.35$ mm

SMR disappears at $\sigma = 1.6$, the response becomes an inter-cavity motion again. According to the best of our knowledge, there is no effective theoretical tool to predict the threshold of SMR occurrence and disappearance under non-natural frequency excitation, which means that Eq. (24) is only valid for σ =0. When the frequency is away from the natural frequency, the system still performs a stable response without impact. The fixed point of this stable periodic response can be described by the framework of the pure cubic NES model.

The stable analytical branch of the VI NES model (circles in Fig. 11b) also fits well to the VIC NES numerical results in the vicinity of the natural frequency when impact occurs. This interval is distinguished by the drastic increase in LO amplitude between [-1.4, 1]. The overlapping of the maximal and average amplitude curves implies a stable response of the system. The separation of both curves indicates the occurrence of a SMR in the frequency interval [1.2, 1.6]. Compared with the pure cubic NES case, this interval is relatively narrow for SMR occurrence.

3.3. Large clearance case

If clearance length b is $>N_{2,2} = 27.4$ mm, this design can be considered as large clearance design. In the simulation, b value is fixed for 30 mm so that the extra singularity line $Z_2 = Z_{2,e3}$ is located on the right stable SIM

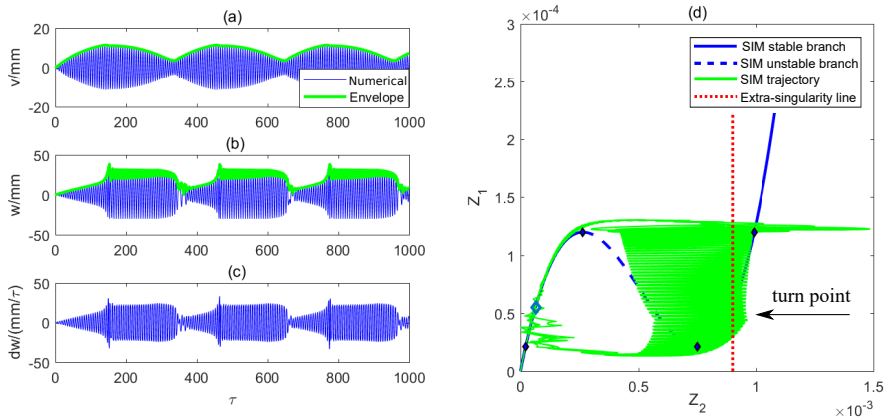

Figure 12: (a),(b) Time displacement response of v and w for large clearance case $G = 0.25$ mm, $\sigma = 0$. The envelopes represent the reconstructed amplitude, while the thin curves describe the time responses (c) velocity of the NES $\dot{w}$ (d) SIM structure and the phase trajectory. The solid/dashed line is a stable/unstable branch of SIM. The dotted straight line is the extra-singularity line.

branch (Fig. 12d). In the lower energy case, the system performs more like a cubic NES. The phase trajectory rises along the left stable SIM branch until the excitation amplitude exceeds the threshold $G_{1,c}$. A large clearance ensures that the influence of the displacement constraint is validated only for the higher energy input case.

The SMR starts at $G = 0.24$ mm, the same as previous cases since displacement constraint has no impact on the SMR occurrence threshold. Figure. 12 presents a classic SMR for $G = 0.25$ mm.

A significant feature of the large clearance case—when compared to the modest case (Fig. 9)—is that the time required for a complete SMR is shorter. The reduction is mainly reflected on the much shorter duration of the 1:1 resonance. An obvious turn point occurs, above which the phase trajectory oscillates along the extra singularity line. Once the phase trajectory descends and crosses the intersection of the extra singularity line and the right SIM branch, the phase trajectory is attracted by the right half-branch of the SIM. In Fig. 12d, the direction of the phase trajectory descent changes at the turning point, from

vertical descent to descent along the SIM.

When $G = 0.44$ mm, the stable amplitude of NES exceeds the b, which interprets that the line with triangle markers has the some distance to stable response predicted by the VI NES model in Fig. 13a. As excitation increases, the final fixed point is located in the extra singularity line instead of in a small part of the SIM stable branch. In the high energy input case, the VI NES model can better predict the fixed point of the VIC NES, so that the two curves approach each other (Fig. 13a).

In the frequency domain, the VI NES model also demonstrates its effectiveness in predicting the fixed point of the VIC NES for $G = 0.6$ mm in Fig. 13. Since excitation is larger, the system has a greater frequency range for collisions between [-4, 3.4]. On the lower frequency side of the impact interval, the theoretically predicted values of the circled points are smaller than the simulated values. On the higher frequency side, theoretical prediction values are larger.

In the large clearance case, collision frequency vanished in the range of [-5, -4.2] and [3.6, 5]. The numerical simulation accurately locates the analytical prediction of the cubic NES model. The SMR frequency is in the range of [1.8,3.4], where the average and maximal amplitude curves start to separate in Fig. 13b. Compared with Fig. 11, the frequency range of the SMR is more significant in this case. The magnitude of the external excitation does not affect the frequency range of SMR appearance in subsequent studies. Thus, the influence on the frequency range variation of SMR appearance can only be due to the change in clearance length.

4. Frequency domain behaviors and optimal design

In the previous section, the frequency distribution of the system under certain excitation conditions was discussed. This section focuses on the frequency distribution of the system under different excitations for modest and large clearance designs.

Figure. 14 shows the transform of response regimes along with frequency

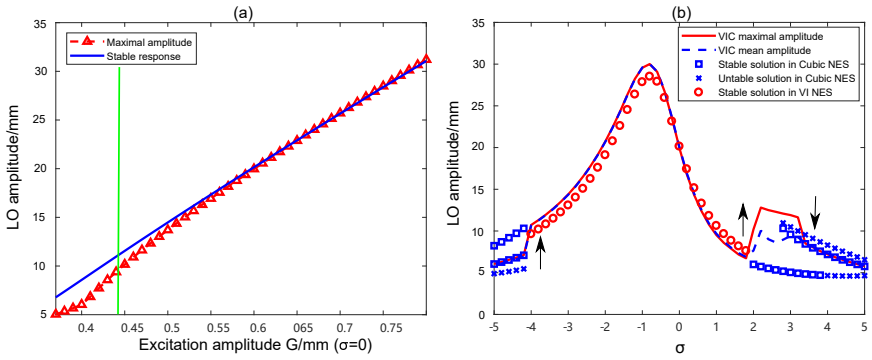

Figure 13: Comparison between the numerical response and analytical prediction (a) in growing excitation case for $\sigma = 0$ and (b) in the frequency domain for $G = 0.6$ mm

increase direction: (1) periodic response without impact, (2) resonance peak, (3) optimal region and (4) SMR region, (5) periodic response without impact. On both the low and high frequency sides, the collision is not ensured even in the high excitation amplitude. The collision boundary comprises the left boundary of the resonance peak and the right side of the SMR region. Collision on the low frequency side results in a sudden increase of the maximum LO amplitude. This case, deemed dangerous, is known as resonance peak. According to its interpretation in the cubic NES system [32], the resonance peak results from a saddle-node bifurcation where the three solutions of Eq. (13) occur. The optimization interval has a shape akin to a valley and is located in the middle of the resonance and SMR. As the excitation amplitude increases, the frequency required for the optimal point (minimal LO amplitude) increases.

The system does not perform a stable amplitude response during the SMR and possesses a large instant amplitude. This region has a narrow width in the frequency domain. The SMR interval shifts to a higher frequency region when a higher excitation amplitude is applied. As the excitation amplitude is constant, the frequency increase causes the system to transition directly from the SMR to the stable response without collision, skipping the stable response phase with collision.

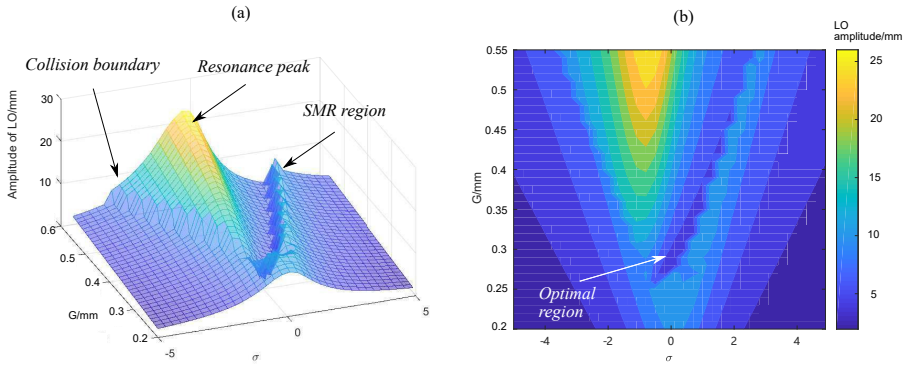

Figure 14: Maximal LO amplitude in the frequency domain for the modest clearance case, b = 22.4 mm. (a) 3D view (b) contour map of maximal LO amplitude.

When the clearance is designed to be larger (Fig. 15), the same characteristic region appears while the collision boundary remains the same (as indicated in Fig. 14). The most dangerous case occurs in G = 0.55 mm, σ = -0.8, whose LO amplitude is maximal (equal to 27.1 mm). Under the same condition, the LO reaches 26.1 mm in a modest clearance case. The smaller clearance design slightly reduces the resonance peak. The optimal region occupies a higher excitation amplitude region, starting from 0.35 mm, while the optimal region in a modest clearance case starts from 0.25 mm. The same increasing frequency behavior can be observed for the optimal region when the excitation increases. A platform appears in the SMR region, being much wider than that of a modest clearance case.

The narrow clearance prevents the phase trajectory from crossing the singularity point $(Z_{2,1}, Z_{1,1})$ in the SIM structure, so the SMR cannot appear in this case. The SMR distributions for the modest, large clearance and cubic cases are shown in 16; the cubic NES case is considered as an infinite long clearance case.

The maximal and average LO amplitudes (and their difference) are calculated to identify the SMR. When the system performs a stable periodic response, both amplitudes are almost the same. If the error between maximal and average

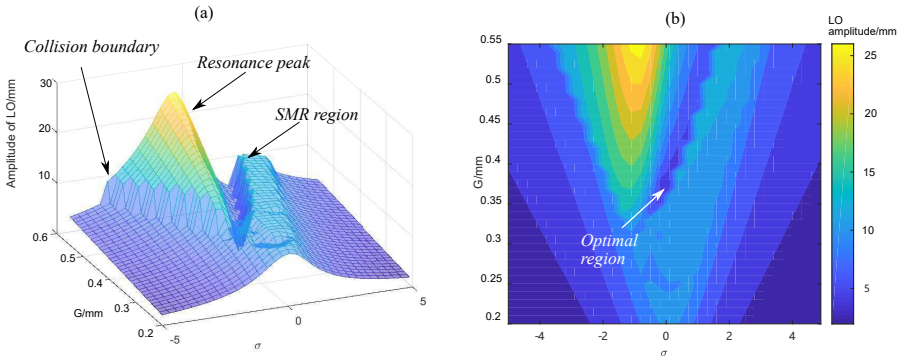

Figure 15: Maximal LO amplitude in the frequency domain for the large clearance case, $b =$ 30 mm. (a) 3D view (b) contour map of maximal LO amplitude.

amplitude is larger than 0.15 mm, the SMR is identified in this condition. Overall, the area where the SMR appears expands with increasing clearance length. The obstruction effect of the impact on SMR emergence is then confirmed. In Fig. 16a, the widest frequency interval is $\sigma =$ [-0.5, 0.7], when $G = 0.265$ mm. Maximal interval in Fig. 16b appears in $\sigma =$ [-1.1, 1] for $G = 0.31$ mm. The cubic NES case shows the largest SMR interval $\sigma =$ [-1.7, 2.2] for $G = 0.37$ mm. As can be seen from the maximal frequency range in which the SMR appears, the displacement constraint reduces the frequency robustness, narrowing the range where the SMR appears.

In the higher energy input cases, the SMR appears on the side where $\sigma >$ 0. The frequency range in which SMR appears on this side remains constant as excitation amplitude increases. The width ranges from 0.3 (Fig. 16a), to 0.9 (Fig. 16b), and then to 2.1 (Fig. 16c). Even at high energy inputs, the frequency range in which SMR appears is also limited by the barrier; the smaller the clearance length, the smaller the frequency range.

Although the SMR region is affected by the clearance length, the thresholds at which SMR appears are all the same, i.e. at $G = 0.22$ mm, $\sigma = 0$. This phenomenon is consistent with our previous observation that clearance length value does not affect the threshold for SMR appearance.

Usually, the cubic nonlinearity and clearance both affect behavior of the VIC

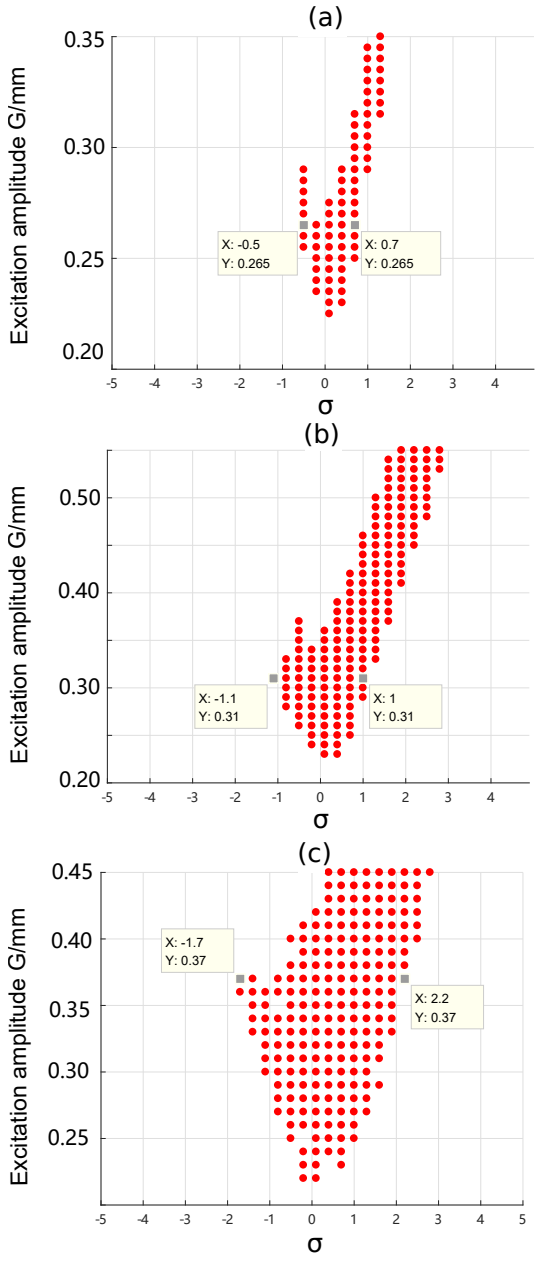

Figure 16: SMR distribution for different clearance length cases (a) $b = 22.4$ mm (b) 30 mm (c) pure cubic case ($b \to \infty$)

NES system simultaneously. However, the dominant parameter has a larger impact depending on the response regimes. For cubic nonlinearity, it plays a more important role during the no-impact condition. The clearance does not influence NES behaviours when NES oscillates inside the gap in a low-energy input case. The fixed point of the no-impact condition is the same as the cubic NES case. In the modest and large clearance design, the cubic nonlinearity has a larger impact on the determination of the excitation threshold for SMR occurrence.

The clearance is more important when the impact occurs in a high energy input case in the following aspects. Firstly, according to the previous analysis, a narrow design ($b<N_{2,1}$) can prevent the occurrence of SMR, and a larger gap also increases the required excitation amplitude to trigger the impact. A modest design ($N_{2,1}<b<N_{2,2}$), clearance length determines required excitation amplitude for SMR disappearance. Secondly, the clearance produces a narrow frequency range of SMR and weaker frequency robustness compared to the cubic NES case. An obvious risk resonance peak is more easily provoked due to clearance on the $\sigma<$ case. Thirdly, impact on the gap provides another effective way to dissipate energy, so the time interval of an SMR cycle turns to be shorter.

4.1. Influence of the restitution coefficient

The restitution coefficient is only valid when there is a collision in the system. The collision thresholds in the narrow clearance case and the modest/large clearance cases where SMR occurs can be seen as the end of the oscillation within the cavity without collision. Therefore, the restitution coefficient has no effect on the start of the collision threshold and the start of the SMR threshold. The threshold predictions of Eq. (14) and Eq. (24) are still valid for different restitution coefficients. The collisions occur in the SMR and stable collision stages, so that the restitution coefficient analysis focuses on the effects in these two stages.

The modest clearance case $b = 22.4$ mm under excitation $G = 0.25$ mm was selected to investigate the role of restitution coefficient. In Fig. 17a, the displacement of three different cases are almost the same due to the absence

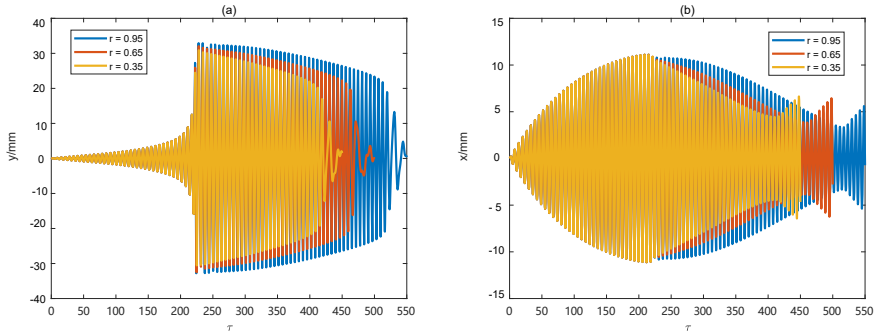

Figure 17: Time displacement response of the SMR for different restitution coefficients r: 0.95, 0.65, and 0.35. (a) absolute displacement of the NES (b) absolute displacement of the LO. The excitation amplitude $G = 0.25$ mm, $\sigma = 0$

of collision. At $\tau = 224$, the NES amplitudes for the three cases sharply and simultaneously increase. In the energy pumping period, the three cases with 0.95, 0.65, and 0.35 coefficients take 295, 239, and 195 times on the τ time scale, respectively. A higher value of restitution coefficient means more energy loss for every impact, accelerating the rate of energy dissipation and leading the system amplitude to decrease more rapidly. This faster amplitude reduction rate is also evident in Fig. 17b. A smaller restitution coefficient enables the system to have more SMR cycles in the same amount of time.

When the system enters the stable impact response (two impacts per cycle), the LO amplitude is governed by the coefficient A_1, B_1, α, β in Eq. (25). The stable analytical amplitude is shown as a solid line in Fig. 18. As restitution coefficient increases, the stable amplitude rises slightly. The numerical results (dot points in Fig. 18) also confirm this tendency. When restitution coefficient varies from 0.8 to 0.3, the stable amplitude is reduced from 12.3 mm to 10.8 mm. This difference cannot be considered as significant when compared to the wide variation range of restitution coefficient. The system shows low sensitivity to the various values of restitution coefficient.

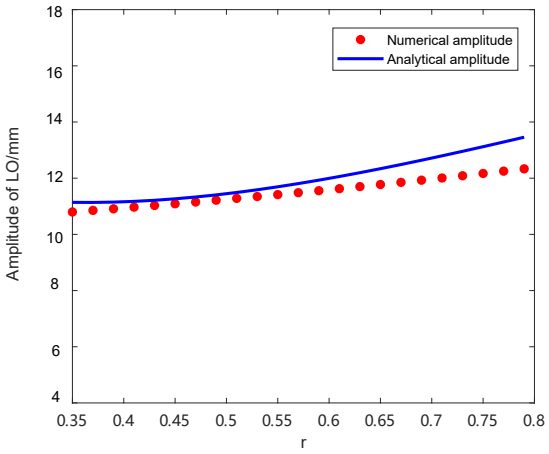

Figure 18: Stable LO amplitudes for various restitution coefficients r under harmonic excitation $G = 0.4$ mm, $\sigma = 0$.

4.2. Clearance design for target excitation

In the previous section, the influence of clearance length has on the different response regimes was presented. Every clearance length design corresponds to a target excitation, under which the LO possesses minimal amplitude.

To find out the corresponding target excitation, various amplitude input cases are applied to the different clearance designs. The corresponding results are shown in Fig. 19. The thin solid lines and thin dashed lines are the maximal and average LO amplitudes, respectively. The diamond-shaped and triangle points correspond to the projection of the local maximal and minimal amplitudes on the b–G plane. The circle points indicate the excitation threshold of SMR occurrence for various clearance length designs. The thick dashed line and thick solid line divide the clearance length designs into three categories, which are classified by singularity value $N_{2,1}$, $N_{2,2}$.

If the clearance length design is $b<N_{2,1} = 16.3$ mm, the snap-through motion is prevented, and the SMR cannot be observed in the first five cases. So the circle points do not appear in the region Fig. 19. The maximal amplitude curve and average amplitude curves are overlapped, which means that the SMR is not

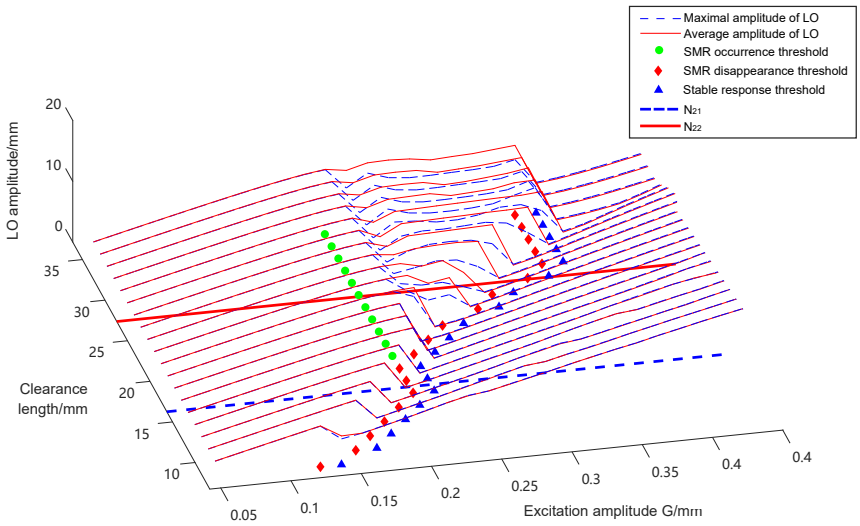

Figure 19: The influence of different clearance length designs on the response regimes. The range of clearance length is [8, 9.5, 11, 12.5, 14, 15.5, 17, 18.5, 20, 21.5, 23, 24.5, 26, 27.5, 29, 30.5, 32, 33.5, 35] mm.

triggered. In those five cases, the response regimes are classified into two types: (1) without impact (2) with impact. In lower energy levels, the NES oscillates within the cavity. The cubic nonlinearity prevents NES mass from contacting the barrier. The threshold of excitation for impact can be calculated by Eq. (14). The occurrence of a collision brings about a sharp drop in amplitude, which can be seen as an optimization point. Local maximal and minimal amplitude points are always adjacent to each other. Before and after impact, the LO amplitude increases almost linearly with excitation.

When the clearance length b designs are $>N_{2,1}$, distance between the extra singularity line $Z_2 = Z_{2,e}$ and the singularity point $Z_2 = Z_{2,1}$ in the SIM structure allows the phase trajectory to feature the snap-through motion. However, the extra singularity line prevents the phase trajectory to arrive on the right SIM stable branch. A complete (classic) SMR cannot occur. As the clearance length b design increases, the SMR appears in a widened amplitude range. So the distance between circle points and triangle points enlarge as clearance length

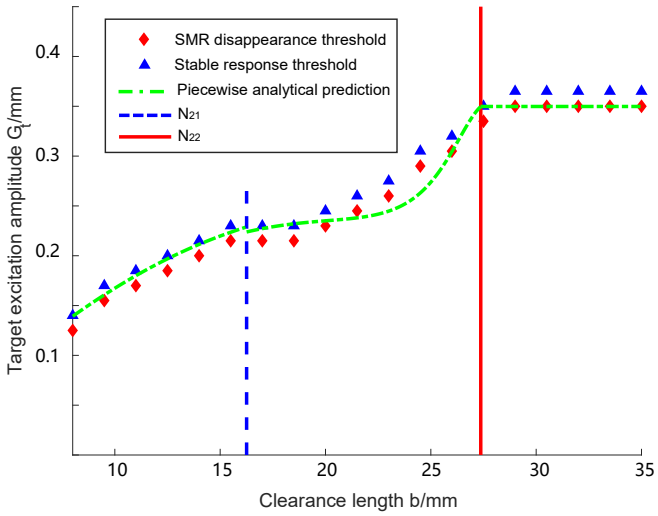

Figure 20: Optimal clearance design for various targeted excitation amplitude

design increases in Fig. 19. The threshold at which SMR appears (as shown by the circle points) remains unchanged. The system changes from a stable response to a SMR to a stable response with collisions as excitation amplitude increases. The local minimal amplitude point occurs after the SMR disappears. A larger displacement constraint can adjust the VIC NES to optimally adapt to a larger excitation.

Once the clearance is designed to be $b{>}N_{2,2} = 27.4$ mm, continuing to increase the gap length has no effect on the threshold for the appearance and end of the SMR. The excitation interval for the presence of SMR remains unchanged in the last four cases, whose clearance lengths are all larger than the critical value $N_{2,2}$. So the distances between circle points and triangle points remain constant as clearance design increases in Fig. 19. In the third category, the clearance design has no influence on the optimal point, which appears at the singularity point $(Z_{2,2}, Z_{1,2})$ in the SIM structure. The gap-enlarging method to increase the amplitude that can be optimally absorbed by the system thus fails.

The distributions of target excitation for different clearance length b designs are shown in Fig. 20 (triangle points). Three types of clearance design are distinguished by thick dashed and solid straight lines. If the excitation amplitude is below the critical value $G_{1,c}$, it can be classified as a low energy input. Therefore, the clearance design that should make the extra singularity line $Z_2 = Z_{2,e}$ is located on the left stable SIM branch. Collision occurs and the system achieves the optimal state when the system oscillates in a maximal amplitude and slightly increases its excitation amplitude. The impact condition for a narrow clearance is derived from Eq. (14), which leads to the optimal curve (dash-dotted line in the left side of $N_{2,1}$). The optimal clearance length b_o can be solved by setting $G_t = \epsilon F_t$ into Eq. (14). The maximal and minimal amplitude points are very close to each other, with the distance being determined by the step size of the excitation amplitude in the numerical simulation. In the ideal case, the maximal and minimal amplitude points are the same and the triangle and diamond-shaped points overlap. Owing to the step size limitation, the triangle and diamond-shaped points distributed on both sides of the optimal curve validate the optimal design in this case.

If the target excitation is within the interval $[G_{1,c}, G_{2,c}]$, the clearance length b should be within the interval $[N_{2,1}, N_{2,2}]$. The clearance length determines the threshold where the SMR disappears, which is also viewed as an optimal state for the LO. The dash-dotted curve is plotted by Eq. (24), demonstrating the optimal clearance design once the target excitation value has been set. When the target excitation nears $G_{1,c}$, the optimal curve is flat and sensitive to target excitation. A slight variation in target excitation G_t would cause the design value of b to increase significantly. When the target excitation nears $G_{2,c}$, the analytical prediction will produce a larger design value, causing the system to perform the SMR. In this design case, the actual optimal clearance should be slightly smaller than the analytical prediction value. In general, the numerical simulations show a linear relationship and the analytical values reveal a quadratic term relationship. However, the analytical solution is still referable to the optimal curve.

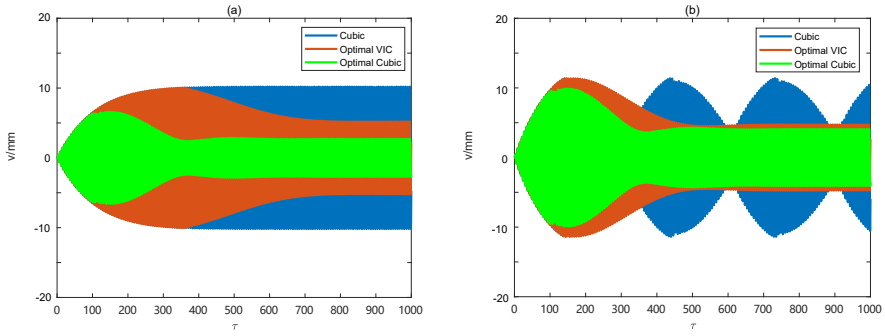

Figure 21: Optimal result for (a) target excitation $G_t = 0.2$ mm, $\sigma = 0$. The optimal clearance length for VIC NES is $b_o = 12.5$ mm, (b) target excitation $G_t = 0.3$ mm, $\sigma = 0$. The optimal clearance length for VIC NES is $b_o = 24$ mm

If the target excitation exceeds $G_{2,c}$, adjusting the clearance length would go beyond adapting the increasing excitation. In other words, if the clearance length is $b > N_{2,2} = 27.4$ mm, the target excitation that system can absorb remains constant $G_t = 0.35$ mm. The final point of phases trajectory will be located at singularity point $(Z_{2,2}, Z_{1,2})$ (optimal state) in the SIM structure, which is independent of the extra singularity line $Z_2 = Z_{2,e}$ (clearance design). On the right side of Fig. 20, the triangle and diamond-shaped points are aligned horizontally. The horizontal analytical curve coincides with the point where the SMR ends. Note that the numerical result slightly exceeds the analytical design value.

The results for the different target excitations are presented in Fig. 21. The cubic nonlinearity parameter of the optimal cubic NES is determined using the method proposed in [34], where the final phase trajectory stays in the singularity point of the SIM.

When $G_t = 0.2$ mm, the cubic NES performs a stable periodic response (amplitude = 10.2 mm in Fig. 21a), whose phase trajectory is finially located on the SIM left branch (as in Fig. 5c). However, the optimal VIC NES has a smaller final LO amplitude for the optimal clearance design $b_o = 12.5$ mm, about 5.2 mm. If the cubic NES is tuned by substituting the original K value (1.742e3)

with an optimal cubic nonlinearity parameter K (6.01e3), the system will hold the minimal LO amplitude (about 2.73 mm). So in a low target excitation case ($G_t < G_{1,c}$), the tuning clearance length can lead to an obvious vibration mitigation performance. However, the replacement of cubic nonlinearity parameter can achieve better performance.

In Fig. 21b, the target excitation is set to 0.3 mm, which is between $[G_{1,c}, G_{2,c}]$. The SMR constitutes the principal motion for the original cubic NES. According to Fig. 20, the optimal clearance design $b_o = 24$ mm minimizes the LO amplitude to 4.75 mm. The SMR will reappear under the target excitation in a larger clearance design. A clearance design $<b_o$ will increase the final stable LO amplitude. The cubic nonlinearity parameter of the original cubic NES K must be tuned to 2.61e3 to achieve a minimal amplitude of 4.06 mm. The optimal cubic NES with the replacement of K represents a not-so-obvious improvement to the optimal VIC NES.

The cubic NES with fixed cubic nonlinearity can only adapt a single target excitation. If the system is under a smaller excitation, a larger cubic nonlinearity parameter K is required for optimal energy absorption. In the real mechanical environment, the replacement of the spring component has a considerable cost and requires a system redesign. Thus, the VIC NES can provide an alternative approach to adapt a weaker target excitation without changing its spring components.

4.3. Frequency performance

The above optimization strategy focuses on the design for harmonic excitation for σ =0, where the optimal state is the periodic solution with minimal LO amplitude. However, this optimal strategy leads to the risk of resonance peak on the σ<0 side, which can be observed in Fig.14,15.

Its absorbing frequency range for cubic and VIC NES in the vicinity of σ =0 is emphasized with the comparison of the tuned mass damper.

To achieve an as broad as possible frequency performance for the target excitation amplitude G = 0.3mm, the cubic nonlinearity parameter K is chosen

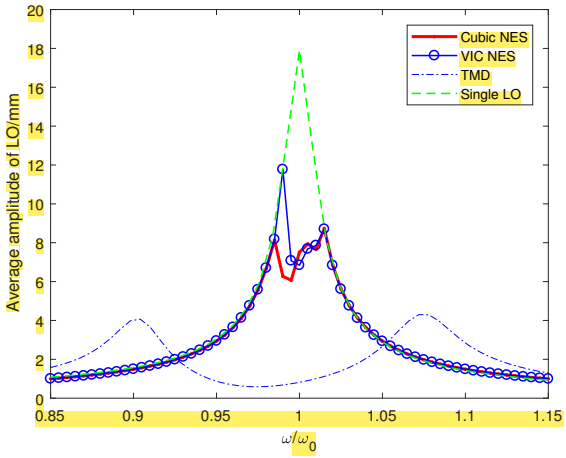

Figure 22: Frequency absorbing performance comparison between cubic NES (thick solid line), VIC NES (dotted line), TMD (dashed-dotted line) and single linear oscillator (dashed line)

as 2.4e3 in the cubic NES, slightly lower than K = 2.61e3 in the last subsection. The VIC NES has applied the same cubic nonlinearity K value, with optimal clearance length b =23.4mm.

As for the corresponding tuned mass damper system, the attached mass m_2 can not be too small to achieve an effective mitigation effect. So the m_2 is selected to 0.15kg in the simulation, whose mass ratio is 0.03, much larger than the mass ratio of the NES case, 0.01. The optimal linear stiffness k_l for attached TMD system is calculated as 112 N/m to satisfy the condition $k_l = \frac{k_1\epsilon}{(1+\epsilon)^2}$. This optimization strategy can be found in [36] to make two resonance peaks equal. The system parameters of LO and TMD damping are the same as with nonlinear systems. Fig.22 shows the frequency responses of three types of absorber, along with a single LO without attached system in the vicinity of $\sigma = 0$.

In Fig.22, the cubic NES can effectively mitigate the vibration near the natural frequency through the strongly modulated response. With the introduction of clearance, the VIC NES causes the resonance peak on the ω/ω_0<0 side. Hence it damages the frequency robustness of cubic NES. With the increasing or decreasing of excitation, the vibration mitigation of NESs is weak, so the three

curves are almost overlapping. The absorb frequency range seems to be narrow due to only the cubic nonlinearity design in our case. However, its frequency robustness can be enhanced by selecting the proper damping combination, and mass ratio [37, 38]. The optimal TMD shows a trade-off characteristic of vibration mitigation. It performs much better in the vicinity of ω/ω_0 =1 than two types of NES. The minimal LO amplitude of the TMD case has been reduced 96.7% of the single LO frequency response peak. Meanwhile, the cubic NES and VIC NES only achieve 66.1% and 61.8% LO amplitude mitigation, respectively. However, two prominent extra peak occurs on the two side of ω/ω_0 =1 due to the introduction of attached mass.

5. Experimental validation

The experimental setup was designed to observe the influence that impact has on the behavior of the SMR distribution. Harmonic excitation is initially applied to the LO structure at a specific range of resonance frequency. The threshold value of SMR occurrence and disappearance and the SMR bandwidth in high energy input cases were recorded.

5.1. Vibro-impact cubic NES construction

The pure cubic nonlinearity is achieved with a four springs system, which is tuned to a specific pre-compression length to avoid the linear stiffness component in the whole combined force-displacement relationship. The detailed construction process is detailed [2]. The cubic NES device is classified into two parts: (1) conical springs mechanism, (2) linear springs mechanism, according to the characteristic of nonlinearity that is provided by different parts of the device.

In the conical springs mechanism, the single conical spring presents a piecewise force-displacement curve: linear phase and nonlinear phase. The transition point divides those two phases during the compression. Once the deflection of spring crosses the transition point, the nonlinear behaviors start. So to overcome the linear stiffness phase, a symmetrical connection type is proposed.

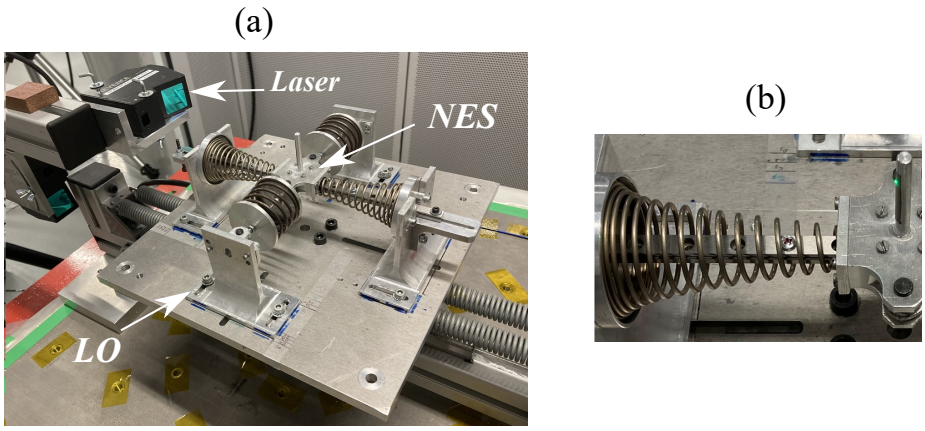

Figure 23: Experimental device (a) construction of NES and LO (b) realization of displacement constraint

The two conical springs are pre-compressed at the transition point. When the center mass moves along the axis of the conical spring, the composed force-displacement curve is smooth and no longer piecewise.

The composed force-displacement curve of conical springs contains a linear stiffness part that prevents the direct application of two conical springs systems. To construct a pure cubic nonlinearity without a linear part, a negative stiffness is implemented through two cylindrical compression springs in the linear springs mechanism. The cylindrical spring can rotate with the other end fixed. The direction of movement is perpendicular to its axis. The linear stiffness of four springs device can be totally counterbalanced through tuning the proper pre-compression length o linear cylindral springs.

The NES mass is attached to the track through the four springs system, so that it can move along the axis of the conical spring. The whole NES system is connected to the LO, which is embedded on a 10 kN electrodynamic shaker. Two perpendicular countless laser sensors are used to measure the displacement of LO and NES, respectively. The experimental setup is presented in Fig. 23.

The two steel screws with galvanised surface are installed in the hole of the track to stop the relative sliding of the NES into creating displacement constraints (Fig. 23b).Due to the design of the track itself, the distance between

Table 1: Experimental parameters of environment

Reduced parameters	ϵ	λ_1	λ_2	K	r	b_1	b_2
	1.2%	1.67	0.167	4.88e3	0.65	11.5 mm	16 mm

each hole is 15 mm. By choosing different mounting positions for the screws or by adjusting the position of the rails, we can obtain different clearance configurations. When impact occurs, the side of the NES mass is in contact with the top of the screw on both sides. The stud of the screw was slightly cut down to avoid coming into contact with the conical spring coils and screws, thus ensuring that the impact only occurs between the screws and NES mass. The parameters of the experimental setup and two types of clearance lengths are given in Tab. 1. The b_1 and b_2 parameters lie within the unstable SIM branch. The restitution coefficient r is measured by connecting the NES to the ground. All the springs are removed to conserve only the NES mass. An initial NES velocity is applied, so that the NES—the velocity measuring instrument—can measure velocity changes before and after the impact. According to its definition, the average value of restitution coefficient can be calculated through 10 time tests.

5.2. Dynamic tests

The amplitude of the harmonic excitation amplitude ranges from 0.18 mm to 0.3 mm, and the difference between the amplitude of adjacent excitation is 0.02 mm. The velocity of frequency sweep is 0.01 Hz/s. Three different clearance cases ($b = 11.5$ mm, $b = 16$ mm and cubic) were chosen to examine the impact effect. The frequency response for the three clearance cases is shown in Fig. 24. The triangle marks the interval of SMR appearance. The variety of SMR regions according to the clearance changes in Fig. 24 shows the same tendency as the numerical simulation in Fig. 16. The adjacent responses are marked in different colours to distinguish between them.

In a low energy input case (e.g. $G = 0.18$ mm), the NES behaviors in Fig. 24 show the same SMR extinction. The maximal amplitude occurs at its natural

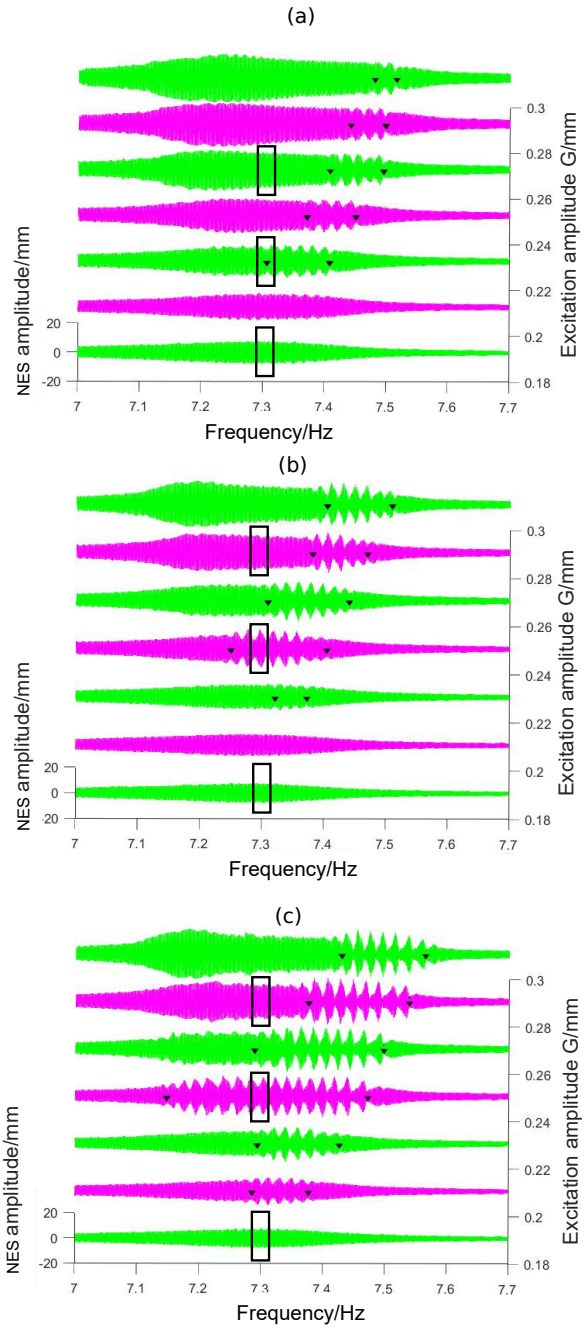

Figure 24: Frequency response of the NES for different clearance case (a)b= 11.5 mm case (b)b = 16 mm case (c) Cubic NES case. The excitation amplitudes are ranged as 0.18 mm 0.2 mm, 0.22 mm, 0.24 mm, 0.26 mm 0.28 mm and 0.3 mm

frequency $f_0 = 7.3$ Hz for 7.61 mm, 7.68 mm and 7.71 mm, respectively. The frequency response of the three cases is almost identical, meaning that impact does not occur.

For a higher amplitude excitation $G = 0.20$ mm, the SMR first occurs in the cubic case (Fig. 24c) for [7.28 Hz 7.38 Hz]. The SMR range is selected by the complete SMR cycle, including the increasing amplitude-phase and decreasing phase. There are no obvious SMR behaviors that appear in this energy input case for both VIC NES cases.

If the excitation reaches 0.22 mm, the obvious SMR behavior occurs in both cases (Fig. 24a-b). In case $b = 11.5$ mm, the SMR appears and reaches its widest frequency bandwidth for [7.31 Hz 7.41 Hz] at the same time. The SMR range of the cubic NES case becomes larger than that of the $G = 0.20$ mm case.

When $G = 0.24$ mm, the SMR range of Fig. 24a remains constant, compared with the previous $G = 0.22$ mm case. In the natural frequency, the response shown in Fig. 24a turns into a periodic response, which is considered as the threshold for SMR disappearance for case $b = 11.5$ mm. Meanwhile the widest SMR frequency bandwidth in Fig. 24b case also reaches at $G = 0.24$ mm for [7.25 Hz, 7.41 Hz]. In the cubic NES, the SMR range also continues to widen until the excitation amplitude equals 0.24 mm, which is where the cubic NES has the widest SMR bandwidth for [7.147 Hz, 7.473 Hz].

When $G = 0.26$ mm, the SMR range width remains constant but is located on a higher frequency side of f_0 in (Fig. 24a). The SMR disappears at its natural frequency $f_0 = 7.3$ Hz in Fig. 24b. Therefore, this case is considered as a threshold for SMR disappearance for case $b = 17$ mm. The SMR range for cubic NES becomes narrower compared to the previous lower amplitude energy case.

For the higher amplitude inputs ($G = 0.28/\ 0.30$ mm), the SMR intervals of the three cases shift to a higher frequency, and a decrease of the SMR range shown in Fig. 24a is observed. In the vicinity of the natural frequency in Fig. 24c, the amplitude of the cubic NES tends to become constant. Thus, the excitation amplitude threshold for SMR disappearance for cubic case is recorded as 0.28

mm.

5.3. Results analysis

For the sake of simplicity, the results of the target phenomena are summarized in Tab. 2. According to the parameter of experiment device, the Z_2 values in the two singularity points are $Z_{2,1}$ = 9.7e-5 and $Z_{2,2}$ = 2.7e-04. The correspond critical clearance value $N_{2,1}$ = 9.7mm and $N_{2,2}$ = 16.4mm. The two clearance length (11.5mm and 16mm) are inside the interval of $[N_{2,2}, N_{2,2}]$. So those two cases are identified as two modest clearance length cases, which allows the occurrence of SMR theoretically. The clearance length does not influence the SMR occurrence threshold $G_{1,c}$ = 0.16mm with the calculation of experiment parameters. Compared with experimental observation, the system has SMR at amplitude G=0.2mm of case(c) and 0.22mm of cases (a) and (b). According to the simulation discussed in the previous section, the clearance length b parameter does not influence SMR occurrence. However, an impact observed in our experimental setup leads to the higher required excitation amplitude to trigger the SMR. Our current theoretical tool states that LO and NES amplitudes reach the singularity point $(Z_{2,1}, Z_{1,1})$ of the SIM to satisfy the SMR triggering conditions. From the energy point of view, a loss of energy ensues once the impact occurs, which may prevent the phase trajectory from fully crossing the singularity line $Z_2 = Z_{2,1}$. The system thus requires more considerable energy (amplitude) excitation to trigger the SMR. This might explains the differences in the excitation threshold for the SMR.

In the cubic NES without displacement constraint, the theoretical amplitude threshold for SMR disappearance $G_{2,c}$ = 0.25mm. Meanwhile, when excitation amplitude achieves 0.28mm, SMR disappears at a natural frequency 7.3Hz in case(c). With influence of clearance length, a larger clearance length in case(b) leads to a lower calculated $G_{2,c}$ 0.25mm, with experimental observation of 0.26mm in Fig.24b. The most narrow clearance case continues to reduce calculated $G_{2,c}$ to 0.17mm, compared with the experimental observation of 0.24mm. Both theoretical analysis and experiment results show that

Table 2: Effect of clearance length on the threshold and SMR distribution

Case	(a)	(b)	(c)
Threshold for SMR occurrence ($\sigma = 0$)	0.22 mm	0.22 mm	0.2 mm
Threshold for SMR disappear ($\sigma = 0$)	0.24 mm	0.26 mm	0.28 mm
Analytical $G_{2,c}$ ($\sigma = 0$)	0.17 mm	0.235 mm	0.25 mm
Widest SMR interval	0.10 Hz	0.16 Hz	0.33 Hz
SMR interval for $G = 0.3$ mm	0.035 Hz	0.106 Hz	0.136 Hz

the larger gap length can raise the critical excitation amplitude for SMR disappearance. The second row in Tab.2 shows an obvious decline in excitation threshold for SMR disappearance. The LO amplitude reaches its local minima when the SMR disappears, which is considered to be an optimal design. By adjusting the clearance length, the VIC NES can be used as an alternative optimal design. The smaller the clearance length, the narrower the widest range of SMR frequency occurrence and the smaller the excitation amplitude threshold value of the SMR disappearance. In the high energy case ($G = 0.3$mm), the SMR frequency interval is reduced as the clearance length decreases. Compared with the cubic NES case, the SMR bandwidth in case (a) is reduced to 25%, and the case (b) is reduced to 78%. The impact influence on SMR frequency distribution is then essential.

The introduction of impact in the cubic NES damages the robustness of the SMR, as confirmed by both the numerical and experimental tests. If the cubic NES system is well tuned, the impact should be avoided. However, if the cubic NES is not well tuned or is under a weaker excitation amplitude, the displacement constraint (impact) would provide an alternative approach to tune the NES, in order to meet the target excitation without modifying the spring components.

The steady-state response can be observed by picking the small interval as the black box in Fig.24. The small time interval of linear sweep experiments corresponds to a steady-state response. In this narrow interval, the excitation

frequency can be considered as an approximate constant. In the vicinity of 7.3Hz, three different responses for single frequency excitation are observed in three clearance designs. With increasing amplitude, the periodic motion, SMR and periodic motion appear in turn. When three systems are under the G=0.18mm, the corresponding NES amplitudes are 7.5mm, 7.4mm, and 7.4mm. The similar NES amplitudes indicate no impact occurrence. At a frequency 7.3Hz, the SMR only occurs for case (a) for G = 0.22mm. When the clearance length enlarges in case(b), SMR appears between G =[0.24 0.26]mm for a natural frequency excitation. When clearance does not exist in case(c), the amplitude range for SMR becomes maximal from G =0.22mm to 0.28mm. Steady-state confirms that a more narrow clearance reduces amplitude range for SMR and effective vibration mitigation effect.

6. Conclusions

This current work investigates a novel NES with both cubic nonlinearity and impact conditions using analytical, numerical and experimental methods. According to the clearance length, the Vibro-Impact Cubic (VIC) NES is naturally classified into narrow, modest, and large clearance cases. The corresponding response regimes under various energy input cases were analyzed, leading to the following conclusions:

1. The impact originating from the barrier introduces an extra singularity line in the Slow Invariant Manifold (SIM) structure. When the system is not impacted, the characteristics of the VIC NES are determined by the cubic nonlinearity. The impact threshold is calculated using the asymptotic method. Once the impact occurs, the ensuing response is closer to the conventional Vibro-Impact (VI) NES. The fixed point of the VIC NES at different harmonic excitation amplitudes and frequencies can be accurately predicted using a simplified VI NES model.
2. Some characteristic regions (e.g. the resonance peak, optimal region and Strongly Modulated Response (SMR) regions) are found in the frequency

domain. The displacement constraint destroys the robustness of the SMR, resulting in a narrower SMR region. A lower value of the restitution coefficient accelerates the energy pumping rate during 1:1 resonance. The fixed point of the system is not sensitive to the variation of restitution coefficient.

3. The optimal clearance designs are concentrated. The target excitation must be smaller than the amplitude threshold $G_{2,c}$ under the framework of the cubic NES in order to make the displacement constraint effective and to absorb energy better than the original design of cubic NES. The piecewise curve of optimal clearance design according to the target excitation is drawn, validated that a lower target excitation requires a narrower clearance length to be tuned as an optimal state.
4. Our experiments confirm the effect that different clearance lengths have on reducing the excitation amplitude threshold for SMR disappearance and on narrowing the SMR frequency interval, which is also obtained by numerical simulation. The target excitation can be adapted optimally by modifying the clearance length. The robustness of SMR in the frequency domain is reduced for a narrower clearance length.

7. Appendix

The expressions Δ, α, β:

$$\Delta = \frac{\sqrt{4-\epsilon^2\lambda^2}}{2}, \alpha = -\frac{\Omega G\lambda\varepsilon^2}{\left(\Omega^2-1\right)^2+\varepsilon^2\lambda^2\Omega^2}, \quad \beta = -\frac{\varepsilon G\left(\Omega^2-1\right)}{\left(\Omega^2-1\right)^2+\varepsilon^2\lambda^2\Omega^2} \tag{25}$$

To solve the integration constant A_1, B_1, C_1, D_1, the expressions given in Eq. (19) are inserted into the half period condition Eq. (28) as solutions with two symmetrical impacts per cycle. The solutions for those integration constants are:

$$
\begin{aligned}
A_1 &= -2(1+R)\left(-\alpha\sin\left(\tau_0\right)+\beta\cos\tau_0\right)\varepsilon\Omega es/I \\
B_1 &= -\frac{A_1(ec+1)}{es} \\
C_1 &= -\Delta\left(2ec+1+\mathrm{e}^{-\varepsilon\lambda\pi/\Omega}\right)(1+R)\left(-\alpha\sin\left(\tau_0\right)+\beta\cos\tau_0\right) \\
D_1 &= -\frac{C_1\pi}{2\Omega}
\end{aligned}
\tag{26}
$$

with

$$
\begin{aligned}
e = \mathrm{e}^{-\epsilon\lambda\pi/(2\Omega)}, s = \sin(\Delta\pi/\Omega), c = \cos(\Delta\pi/\Omega) \\
I = -\varepsilon^2\lambda(1+R)es + 2R\varepsilon\Delta e(e-c) - 2\Delta\varepsilon(ec+1) \\
-\Delta\left(1+e^2\right) + 2\Delta ec(R-1) + \Delta R\left(1+e^2\right)
\end{aligned}
\tag{27}
$$

As with the solutions with two symmetrical impacts per cycle, we can also consider a half period:

$$
\begin{aligned}
X(0) = X_0, X(\pi/\Omega) = -X_0, Y(0) = Y_0, Y(\pi/\Omega) = -Y_0 \\
\dot{X}_+(0) = \dot{X}_0, \dot{X}_+(\pi/\Omega) = -\dot{X}_0, \dot{Y}_+(0) = \dot{Y}_0, \dot{Y}_+(\pi/\Omega) = -\dot{Y}_0
\end{aligned}
\tag{28}
$$

Re-substituting Eq. (28) into the initial condition $|X-Y|=1$ yields the expression of initial time η:

$$
\eta = \arctan\frac{b_1}{a_1} \pm \arccos\frac{1}{\sqrt{a_1^2+b_1^2}} \tag{29}
$$

where a_1 and b_1 are voluminous and only their appearances are presented.

The η value corresponds to two fixed points.The detailed calculation can be also found in [9].

8. Acknowledgements

The authors acknowledge the China Scholarship Council under Grant No. 201801810128 for their financial support.

9. Declaration

The authors have no conflicts of interest to declare that are relevant to the content of this article.

10. Author statement

Zhenhang Wu: Formal analysis, methodology and writing - original draft **Manuel Paredes**: Supervision, experiment advice and writing - review & editing. **Sébastien Seguy**: Supervision, conceptualization and writing - review & editing.

References

[1] A. F. Vakakis, Inducing passive nonlinear energy sinks in vibrating systems, J. Vib. Acoust. 123 (3) (2001) 324–332.

[2] D. Qiu, S. Seguy, M. Paredes, Tuned nonlinear energy sink with conical spring: design theory and sensitivity analysis, Journal of Mechanical Design 140 (1).

[3] F. Romeo, L. Manevitch, L. Bergman, A. Vakakis, Transient and chaotic low-energy transfers in a system with bistable nonlinearity, Chaos: An Interdisciplinary Journal of Nonlinear Science 25 (5) (2015) 053109.

[4] T. Li, S. Seguy, A. Berlioz, On the dynamics around targeted energy transfer for vibro-impact nonlinear energy sink, Nonlinear Dynamics 87 (3) (2017) 1453–1466.

[5] B. Youssef, R. I. Leine, A complete set of design rules for a vibro-impact nes based on a multiple scales approximation of a nonlinear mode, Journal of Sound and Vibration 501 (2021) 116043.

[6] A. S. Saeed, M. A. AL-Shudeifat, A. F. Vakakis, W. J. Cantwell, Rotary-impact nonlinear energy sink for shock mitigation: analytical and numerical investigations, Archive of Applied Mechanics 90 (3) (2020) 495–521.

[7] O. Gendelman, G. Sigalov, L. Manevitch, M. Mane, A. Vakakis, L. Bergman, Dynamics of an eccentric rotational nonlinear energy sink, Journal of applied mechanics 79 (1).

[8] J. Wang, C. Zhang, H. Li, Z. Liu, Experimental and numerical studies of a novel track bistable nonlinear energy sink with improved energy robustness for structural response mitigation, Engineering Structures 237 (2021) 112184.

[9] E. Gourc, G. Michon, S. Seguy, A. Berlioz, Targeted energy transfer under harmonic forcing with a vibro-impact nonlinear energy sink: analytical and experimental developments, Journal of Vibration and Acoustics 137 (3).

[10] A. Tripathi, P. Grover, T. Kalmár-Nagy, On optimal performance of nonlinear energy sinks in multiple-degree-of-freedom systems, Journal of Sound and Vibration 388 (2017) 272–297.

[11] R. Bellet, B. Cochelin, P. Herzog, P.-O. Mattei, Experimental study of targeted energy transfer from an acoustic system to a nonlinear membrane absorber, Journal of Sound and Vibration 329 (14) (2010) 2768–2791.

[12] Y. Starosvetsky, O. Gendelman, Strongly modulated response in forced 2dof oscillatory system with essential mass and potential asymmetry, Physica D: Nonlinear Phenomena 237 (13) (2008) 1719–1733.

[13] L. Manevitch, The description of localized normal modes in a chain of nonlinear coupled oscillators using complex variables, Nonlinear Dynamics 25 (1) (2001) 95–109.

[14] O. Gendelman, Y. Starosvetsky, M. Feldman, Attractors of harmonically forced linear oscillator with attached nonlinear energy sink i: description of response regimes, Nonlinear Dynamics 51 (1) (2008) 31–46.

[15] R. A. Ibrahim, Vibro-impact dynamics: modeling, mapping and applications, Vol. 43, Springer Science & Business Media, 2009.

[16] V. I. Babitsky, Theory of vibro-impact systems and applications, Springer Science & Business Media, 2013.

[17] E. Gourc, S. Seguy, G. Michon, A. Berlioz, B. Mann, Quenching chatter instability in turning process with a vibro-impact nonlinear energy sink, Journal of Sound and Vibration 355 (2015) 392–406.

[18] O. Gendelman, Analytic treatment of a system with a vibro-impact nonlinear energy sink, Journal of Sound and Vibration 331 (21) (2012) 4599–4608.

[19] O. Gendelman, A. Alloni, Dynamics of forced system with vibro-impact energy sink, Journal of Sound and Vibration 358 (2015) 301–314.

[20] P. František, More detail view on the dynamics of the impact damper, Facta Universitatis: Mechanics, Automatic Control and Robotics 3 (14) (2003) 907–920.

[21] T. Li, E. Gourc, S. Seguy, A. Berlioz, Dynamics of two vibro-impact nonlinear energy sinks in parallel under periodic and transient excitations, International Journal of Non-Linear Mechanics 90 (2017) 100–110.

[22] P. Thota, X. Zhao, H. Dankowicz, Co-dimension-Two Grazing Bifurcations in Single-Degree-of-Freedom Impact Oscillators, Journal of Computational and Nonlinear Dynamics 1 (4) (2006) 328–335.

[23] P. Thota, H. Dankowicz, Continuous and discontinuous grazing bifurcations in impacting oscillators, Physica D: Nonlinear Phenomena 214 (2) (2006) 187–197.

[24] Y. S. Lee, F. Nucera, A. F. Vakakis, D. M. McFarland, L. A. Bergman, Periodic orbits, damped transitions and targeted energy transfers in oscillators with vibro-impact attachments, Physica D: Nonlinear Phenomena 238 (18) (2009) 1868–1896.

[25] D. Qiu, S. Seguy, M. Paredes, Design criteria for optimally tuned vibro-impact nonlinear energy sink, Journal of Sound and Vibration 442 (2019) 497–513.

[26] Y. Wei, X. Dong, P. Guo, Z. Peng, W. Zhang, Enhanced targeted energy transfer by vibro impact cubic nonlinear energy sink, International Journal of Applied Mechanics 10 (06) (2018) 1850061.

[27] M. Farid, Dynamics of a hybrid cubic vibro-impact oscillator and nonlinear energy sink, arXiv preprint arXiv:2106.02123.

[28] J. Wang, B. Wang, Z. Liu, H. Li, C. Zhang, Seismic response mitigation of building structures with a novel vibro-impact dual-mass damper, Engineering Structures 215 (2020) 110673.

[29] V. Pilipchuk, Closed-form solutions for oscillators with inelastic impacts, Journal of Sound and Vibration 359 (2015) 154–167.

[30] G. F. d. S. Reboucas, I. F. Santos, J. J. Thomsen, Validation of vibro-impact force models by numerical simulation, perturbation methods and experiments, Journal of Sound and Vibration 413 (2018) 291–307.

[31] T. Li, D. Qiu, S. Seguy, A. Berlioz, Activation characteristic of a vibro-impact energy sink and its application to chatter control in turning, Journal of Sound and Vibration 405 (2017) 1–18.

[32] E. Gourc, G. Michon, S. Seguy, A. Berlioz, Experimental investigation and design optimization of targeted energy transfer under periodic forcing, Journal of Vibration and Acoustics 136 (2).

[33] G. Habib, F. Romeo, The tuned bistable nonlinear energy sink, Nonlinear Dynamics 89 (1) (2017) 179–196.

[34] Z. Wu, S. Seguy, M. Paredes, Basic constraints for design optimization of cubic and bistable nonlinear energy sink, Journal of Vibration and Acoustics 144 (2).

[35] F. Peterka, Bifurcations and transition phenomena in an impact oscillator, Chaos, Solitons & Fractals 7 (10) (1996) 1635–1647.

[36] S. Krenk, Frequency Analysis of the Tuned Mass Damper, Journal of Applied Mechanics 72 (6) (2005) 936–942. arXiv:https://asmedigitalcollection.asme.org/appliedmechanics/article-pdf/72/6/936/5473041/936_1.pdf, doi:10.1115/1.2062867. URL https://doi.org/10.1115/1.2062867

[37] M. Parseh, M. Dardel, M. H. Ghasemi, Performance comparison of nonlinear energy sink and linear tuned mass damper in steady-state dynamics of a linear beam, Nonlinear Dynamics 81 (4) (2015) 1981–2002.

[38] G.-X. Wang, H. Ding, Mass design of nonlinear energy sinks, Engineering Structures 250 (2022) 113438.